CHARLES UNIVERSITY IN PRAGUE
FACULTY OF MATHEMATICS AND PHYSICS

Master Thesis

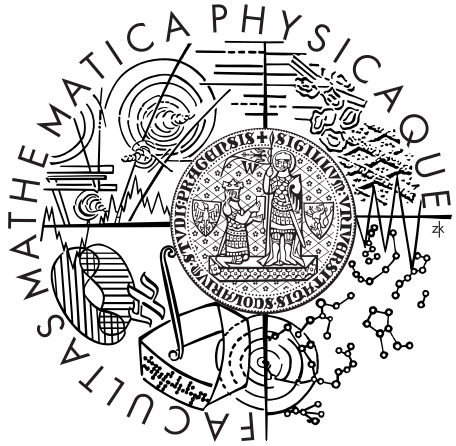

MARTINA ULVROVÁ

Equilibration between sinking metal droplets and molten silicates in magma oceans

Departement of Geophysics

Supervisors: Jakub Velímský & Nicolas Coltice
Study program: Geophysics

2008

Here, I would like to express thanks to all members of both departments Department of Geophysics in Prague and Department of Earth Sciences in Lyon where I worked on my thesis.

My grateful thanks belong to Ondřej Šrámek, Yanick Ricard, Ctirad Matyska, Ladislav Hanyk, Ondřej Souček and Ondřej Čadek who contributed with different but important pieces to the origin of this work. Special thanks belong to Fabien Dubuffet for his kindly help, patience and enthusiasm.

My greatest and most sincere thanks belong to my supervisors, to Jakub Velímský for his help, optimism and critical notes and to Nicolas Coltice, the best teacher I have ever met, for all discussions, his motivation and encouragement.

Finally, I want to thank to Štepán Roučka, my friends, my family and my boyfriend Petr for supporting me.

Prohlašuji, že jsem svou diplomovou práci napsala samostatně a výhradně s použitím citovaných pramenů. Souhlasím se zapůjčováním práce a jejím zveřejňováním.

V Praze dne 18.dubna 2008 Martina Ulvrová

Contents

1 Introduction **6**

2 Physical Model **9**
2.1 Model description 9
2.2 Geometry 11
2.3 Boundary conditions 11
2.3.1 Boundary conditions at the metal-silicate interface 12
2.3.2 Boundary conditions at the external boundary 12
2.4 Velocity field 12
2.4.1 Equation of motion 13
2.4.2 Geometry 13
2.4.3 Limit and boundary conditions 14
2.4.4 Solution 15
2.5 Dimensionless formulation 18
2.6 Analytical model 18
2.7 Parameters of the model 21

3 Numerical Model **25**
3.1 Finite volume formulation 25
3.2 Time-integration scheme 28
3.2.1 Crank-Nicolson Scheme 28
3.2.2 ADI 28
3.3 Discretization of the boundary conditions 30
3.3.1 Discretization at the metal-silicate interface 30
3.3.2 Discretization at the external boundary 31
3.4 Resolution 31
3.5 Benchmarking 31
3.5.1 Benchmark of the diffusion scheme 32
3.5.2 Benchmark of the advection scheme 33

4 Results **35**
4.1 Numerical experiments 35
4.2 Liquid vs. rigid blob 37

5 Discussion **42**

6 Conclusions **45**

A Differential operators in axi-symmetric spherical coordinates **47**

Název práce: Studium rovnováhy mezi klesajícími kapkami železa a roztavenými silikáty v magmatických oceánech
Autor: Martina Ulvrová
Katedra: Katedra geofyziky, MFF UK v Praze
Vedoucí diplomové práce: RNDr. Jakub Velímský, Ph.D.
e-mail vedoucího: velimsky@karel.troja.mff.cuni.cz
Vedoucí diplomové práce: Nicolas Coltice
e-mail vedoucího: coltice@univ-lyon1.fr
Abstrakt: V rané historii Země dochází k tvorbě magmatických oceánů umožňujících separaci kovů a silikátů. Železo následně vytváří kapky a díky hustotnímu rozdílu klesá na dno roztaveného magmatu. V předkládané práci studujeme proces ekvilibrace mezi rozptýlenými železnými kapkami a okolními silikáty, ke kterému dochází makroskopickým transportem látky a mikroskopickou difúzí na rozhraních kapalin. Kapku aproximujeme koulí, která stacionárně padá v okolní kapalině a modelujeme chemický vývoj tohoto heterogenního systému pomocí vytvořeného numerického kódu v axisymetrických sférických souřadnicích. Zaměřujeme se na stanovení časových škál, pro které předkládáme analytický model založený na analýze hraniční vrstvy. Získané charakteristické časy jsou především pro nízké viskozity silikátů velmi kratké, což nasvědčuje tomu, že během klesání kapek bylo dosaženo rovnováhy.
Klíčová slova: Rovnováha silikátů a kovů; Tvorba jádra; Diferenciace

Title: Equilibration between sinking metal droplets and molten silicates in magma oceans
Author: Martina Ulvrová
Department: Department of Geophysics, Charles University in Prague
Supervisor: RNDr. Jakub Velímský, Ph.D.
Supervisor's e-mail address: velimsky@karel.troja.mff.cuni.cz
Supervisor: Nicolas Coltice
Supervisor's e-mail address: coltice@univ-lyon1.fr
Abstract: During the Earth's accretion process deep magma oceans were episodically formed. Differentiation of iron took place within the melted zone and small droplets of iron were sinking to the base of the magma ocean due to the density contrast. In the present work we study the process of equilibration between dispersed metal droplets and surrounding silicates that proceeds by the advection transport and diffusion at the rim. We allow for steady state flow of a spherical liquid blob falling in a host liquid and establish the numerical code in axisymmetric spherical coordinates computing the chemical evolution of such heterogeneous system. We focus on determining the time scales of equilibration for which we propose an analytical model based on the boundary layer analysis. The obtained characteristic times are especially for low silicate viscosities very short that supports the idea that the drops attained equilibrium while sinking.
Keywords: Metal-silicate equilibration; Core-formation; Differentiation

Chapter 1

Introduction

Geophysics, geochemistry and geology interweave in order to discover the Earth's history as well as history of other planetary bodies. One of the most challenging stories involves the history of first tens of millions of years when primitive Earth experienced the most dramatic event throughout its whole history, the core formation. Relevant models of the formation of the core were suggested for the first time in late eighties by Stevenson [23].

Formation of the core involved separation of dense iron from lighter silicates. However, extensive melting of the Earth's interior is required since solid silicate matrix is impermeable for iron alloys within low pressure and temperature conditions. Recent experimental and computational results indicate that large impacts produced enough heating to cause melting and formation of magma oceans on Earth [25].

As pointed out above, extensively melted part of Earth originated in metal separation. Since the surface tension of iron is high (roughly $15\times$ higher than the surface tension of water at a temperature of $50^{\circ}\mathrm{C}$), small iron droplets are formed and fall due to the density contrast taking other elements that concentrate in metal rather than in silicates with them. The droplets fall until they reach the base of the magma ocean where the temperature is below the peridotite liquidus. After sufficiently large volumes have accumulated to overcome the viscous resistance, the metal further percolates in a form of large diapirs to form the core [20]. The rainfall of small droplets and subsequent storage on the rheological boundary are the dominant mechanisms that designate the traces of core formation in today's mantle composition [21].

Important chemical constraints are provided by abundances of siderophile elements. The distribution of elements in the Earth can be understood by measuring the partition coefficient K defined as a ratio of concentration of an element between the metallic phase and the silicate phase. For the partition coefficient of siderophile elements holds $K > 1$. Further, different subclasses are introduced, including the slightly siderophile elements (SDE) for which holds $1 < K < 10$, moderately siderophile elements (MSE) with $10 < K < 10^4$ and highly siderophile elements (HSE) with $K > 10^4$.

Generally, siderophile elements are from one to three orders overabundant in the Earth's upper mantle compared to predictions based on low pressure experiments [18].

Those discrepancies led many scientists to investigate element partitioning within high temperature and pressure ranges. From many papers concerning this topic let us mention [3], [4] [12] and [19].

Changes in partitioning behaviour and subsequent chemical equilibration of metal drops and/or equilibration of metal on the base of the magma ocean is one of possible models how to explain the so-called "excess siderophile element problem". Other hypotheses of core formation that could lead to such siderophile elements abundances are the heterogeneous accretion and late veneers, the inefficient core formation, the addition of core material to the lower mantle and the equilibrium partitioning between sulfur-rich metal and silicate. The basic overview is provided in [10], [21] and [24]. However, none of the hypotheses is able to explain all observations. For example, the high temperature and pressure equilibration in the deep magma ocean solves excess of MSE but still needs the late veneer in order to explain the HSE abundances.

The thermodynamical properties of the magma ocean present more appealing unanswered questions. Temperature, pressure and oxidation state are the crucial parameters of the early Earth. However, different conditions were suggested. Based on partitioning experiments, the temperature range varies between 2000-4000 K and the pressure is estimated to be up to 60 GPa [3].

An important parameter which seems to significantly control dynamic processes in the magma ocean is the viscosity of silicates. However, the viscosity of the magma ocean is not well known, we can only say that it varies in a very broad range depending mainly on temperature. Unfortunately, there are no experimental data for the viscosity within high temperature and pressure conditions and extrapolation of experiments within low conditions is misleading [22].

These questions provide great challenge to contribute to the story of the primitive Earth. We aim to focus the research on understanding the metal "rainfall" by the methods of numerical simulations. More precisely, we investigate the way of chemical equilibration of small droplets settling in the magma ocean in order to derive the scalings for the characteristic times of equilibration.

Numerical models play a crucial role in the core forming scenarios since there is no direct record of this dramatic event and experimental conditions corresponding to the deep magma ocean are so far not possible to produce.

The model is presented and detailed in the second chapter of this work where we present as well an analytical model of the chemical evolution of the system based on the boundary layer analysis.

In order to explore the dynamics of equilibration we build a numerical code that allows to study the evolution of concentration of the element partitioning. Numerical concepts are presented in the third chapter. We also give detailed description of the finite volume method used in the spatial domain and the alternating direction implicit (ADI) method used in the temporal domain.

In chapter 4 we present our results. In arranging numerical experiments we focus on determining the role of silicate viscosity since the viscosity designates the dynamics of the magma ocean.

Finally, in chapter 5 we analyse the attained results and discuss the implications that we sum up in the last chapter 6.

Chapter 2

Physical Model

In this chapter we present our approach to the problem of dispersed metal droplets and their equilibration with the surrounding silicates in the magma ocean. Principal concept of our model is based on the paper of Grasset and Albarede [9] who were studying the mingling of basaltic and felsic magmas, namely their rate of homogenization.

We describe the model and introduce the governing equations. We analyse the terms and envisage the boundary conditions at interfaces. We derive an analytical solution of velocity field for steady state motion of two immiscible liquids and compare it with the velocity field of solid sphere in a liquid medium. Further, we write the equations in dimensionless form and present an analytical model of equilibration of the drop. Finally, we give the plausible ranges of parameters describing the drop settling and bring an analysis of the velocity field within and outside the drop.

2.1 Model description

We consider a single metallic drop falling in a host silicate magma with a constant terminal velocity U_t, exploring thus a steady state motion reached after a certain time passes. A drop neither sways nor rotates.

The two liquids are considered to be immiscible. Next, all equations are derived for incompressible matter, conservation of mass thus reduces to non-divergence of velocity $\boldsymbol{v}$

$$\nabla \cdot \boldsymbol{v} = 0\,. \tag{2.1}$$

Finally, we assume that the drop has a spherical shape and no deformation occurs in course of time evolution.

We aim to model the time evolution of concentration of a given chemical element in the silicate mantle and in the metal drop. Generally, concentration C can vary due to local production of concentration H_C or due to transport across the interface. The transport can proceed by a macroscopic advection flow or by a microscopic diffusion. Below we analyze both of these mechanisms.

Diffusion is a molecular transport that occurs when any variation in concentration is presented. Exchange of atoms by diffusion between two materials is then given by

the same laws as those that describe the transfer of heat by conduction. Namely, the diffusive flux $\boldsymbol{F}_{\mathrm{dif}}$ follows the Fick's law

$$\boldsymbol{F}_{\mathrm{dif}} = -D\nabla C\,, \tag{2.2}$$

where D is a diffusion coefficient. The minus sign indicates that the flux proceeds from regions of higher to regions of lower concentration.

Net rate $\boldsymbol{F}_{\mathrm{adv}}$ at which concentration is flowing obeys the law

$$\boldsymbol{F}_{\mathrm{adv}} = C\boldsymbol{v}\,. \tag{2.3}$$

The total flux is then the sum of advective and diffusive flux $\boldsymbol{F}_{\mathrm{tot}} = \boldsymbol{F}_{\mathrm{dif}} + \boldsymbol{F}_{\mathrm{adv}}$.

Let us consider an arbitrary volume V. The number of particles entering and leaving the volume per unit time that passes through the surface S surrounding the volume V is

$$Q = -\int_S \boldsymbol{F}_{\mathrm{tot}}\,\mathrm{d}\boldsymbol{S}\,. \tag{2.4}$$

Positive direction is chosen outward from the surface.

Change of the number of particles in the volume V per second is $\int_V \partial_t C\,\mathrm{d}V$, where ∂_t denotes time derivation. Equating this to the number entering the volume through its surface (2.4) and using the Gauss theorem to convert the surface integral to the volume integral we obtain

$$\int_V \frac{\partial C}{\partial t}\,\mathrm{d}V = -\int_V \nabla\cdot\boldsymbol{F}_{\mathrm{tot}}\,\mathrm{d}V\,. \tag{2.5}$$

Because the volume V was chosen arbitrarily and adding the volume concentration sources H_{C} to the balance the general conservation equation for concentration leads to

$$\frac{\partial C}{\partial t} = -\nabla\cdot\boldsymbol{F}_{\mathrm{tot}} + H_{\mathrm{C}} = \nabla\cdot(D\nabla C - \boldsymbol{v}C) + H_{\mathrm{C}}\,. \tag{2.6}$$

Eq. (2.6) holds in both media but we allow for different diffusion coefficients D^{I}, D^{II} and velocity fields $\boldsymbol{v}^{\mathrm{I}}$, $\boldsymbol{v}^{\mathrm{II}}$. Since there are no volume concentration sources,

$$\frac{\partial C^{\mathrm{I}}}{\partial t} = -\nabla\cdot\boldsymbol{F}^{\mathrm{I}}_{\mathrm{tot}} = \nabla\cdot(D^{\mathrm{I}}\nabla C^{\mathrm{I}} - \boldsymbol{v}^{\mathrm{I}}C^{\mathrm{I}})\,, \tag{2.7}$$

holds for concentration C^{I} of an element in the metal drop. Likewise, we write for its concentration C^{II} in the silicate magma,

$$\frac{\partial C^{\mathrm{II}}}{\partial t} = -\nabla\cdot\boldsymbol{F}^{\mathrm{II}}_{\mathrm{tot}} = \nabla\cdot(D^{\mathrm{II}}\nabla C^{\mathrm{II}} - \boldsymbol{v}^{\mathrm{II}}C^{\mathrm{II}})\,. \tag{2.8}$$

Dynamical model of chemical equilibration is established in order to explore partitioning of elements between silicates and iron. Below we depicture applied spatial alignment.

2.2 Geometry

The pattern of the task suggests using spherical coordinates. We set the origin at the center of the spherical drop, therefore the motionless drop is seeing lighter magma moving up. As there is an axial symmetry we have two independent variables describing the system, namely a radius r being the distance from the origin and an angle θ measured anti-clockwise from the point of incidence of two liquids, cf. Figure 2.1.

The thickness of the diffusion boundary layer δ in the surrounding silicates is of order of $\sim (D^{\mathrm{II}}R/U_{\mathrm{t}})^{1/2}$, where R is the radius of the blob. Since D^{II} is a low order number ($\sim 10^{-8}\,\mathrm{m^2 s^{-1}}$) boundary layer is much smaller than the radius of the blob, $\delta \ll R$, that allows us to replace infinite space around the blob by a sphere with radius $2R$. We thus assume no chemical influence by diffusion beyond $r = 2R$, cf. Figure 2.1.

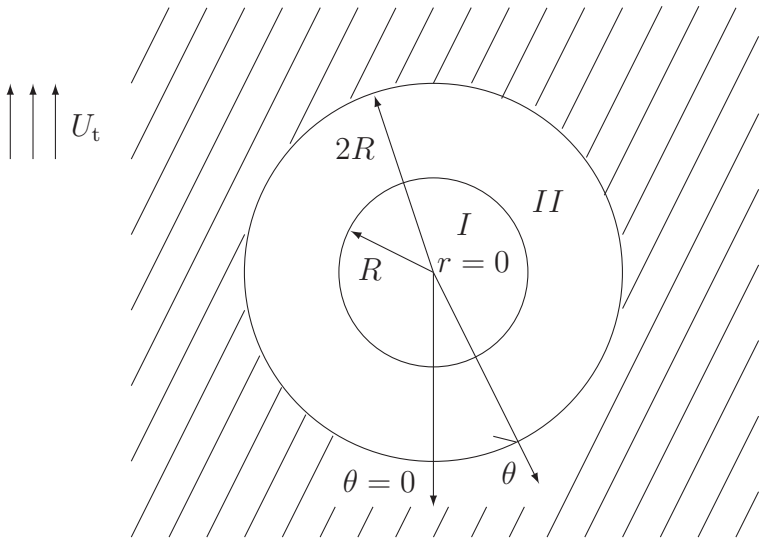

Figure 2.1: The model geometry. The lighter magma ocean is moving up around the denser metal blob with the terminal velocity U_{t}. The origin of the coordinate system is at the centre of the drop. θ is measured anti-clockwise from the point of incidence of two liquids. Diffusion-advection equations are solved in the sphere with radius $2R$.

2.3 Boundary conditions

As we described above there are two boundaries. The first one, at $r = R$, is a material boundary between the silicates and the metallic blob. The second one, at $r = 2R$, is an external no-material boundary. To complete the formulation we need to prescribe boundary conditions.

2.3.1 Boundary conditions at the metal-silicate interface

At the interface between the drop and the magma we impose continuity of normal component of the flux (2.9). No matter is thus accumulated on the boundary

$$[\boldsymbol{F} \cdot \boldsymbol{e}_r]_-^+ = 0 \mid_{r=R} , \tag{2.9}$$

where $\boldsymbol{e}_r$ is a unit vector in the radial direction.

Secondly, we prescribe the partition coefficient K of a compound, we thus define the ratio of concentration of an element between metallic phase and silicate phase at chemical equilibrium

$$K = \frac{C^{\mathrm{I}}}{C^{\mathrm{II}}} \mid_{r=R} . \tag{2.10}$$

Because there is no radial velocity on the boundary (see Eq. (2.31) below), condition (2.9) simplifies as

$$\left[D \frac{\partial C}{\partial r} \right]_-^+ = 0 \mid_{r=R} . \tag{2.11}$$

2.3.2 Boundary conditions at the external boundary

The external boundary is not a material boundary, therefore the conditions imposed on it should not depend on the chosen geometry.

At the front of the drop, for $\theta \in (0, \frac{\pi}{2})$, we keep concentration constant as there is no interaction between blob and magma

$$C = C_{\mathrm{ext}} \mid_{r=2R, \theta < \frac{\pi}{2}} . \tag{2.12}$$

At the leeward side, for $\theta \in (\frac{\pi}{2}, \pi)$, we impose the permeability of the boundary, we thus allow chemical elements to be shifted out. Since the distance $r = 2R$ is far from the diffusion boundary layer δ we impose the condition of zero diffusion flux in the direction of flow

$$\left(D^{\mathrm{II}} \frac{\boldsymbol{v}}{|\boldsymbol{v}|} \cdot \nabla C \right) = 0 \mid_{r=2R, \theta > \frac{\pi}{2}} , \tag{2.13}$$

where $|\boldsymbol{v}|$ is a magnitude of velocity. We thus assume that elements at the boundary are transported only by advection. After simplification we get

$$(\boldsymbol{v} \cdot \nabla C) = 0 \mid_{r=2R, \theta > \frac{\pi}{2}} . \tag{2.14}$$

2.4 Velocity field

In order to solve Eqs. (2.7) and (2.8) a velocity field within and outside the drop for steady state motion must be prescribed. Let us consider two immiscible liquids with different densities and viscosities. A drop that is not deformed and keeps its shape is

falling down due to a gravity force at a certain terminal velocity U_t. We assume motion in a viscous regime, inertia force is thus neglected. After a certain time it reaches a steady motion, there is no acceleration.

To derive the velocity field of the liquid drop in the liquid medium, we consider the continuity equation for an incompressible fluid (2.1) and the Navier-Stokes equation for steady motion [11].

2.4.1 Equation of motion

Because inertia force is neglected, equation of motion

$$\nabla \cdot \boldsymbol{\sigma} + \rho \boldsymbol{g} = 0 \tag{2.15}$$

represents balance between surface and volume forces. Here $\boldsymbol{\sigma}$ and $\boldsymbol{g}$ are viscous stress tensor and gravity acceleration, respectively. In a newtonian incompressible fluid the rheological relation reads as

$$\boldsymbol{\sigma} = -P\boldsymbol{I} + \mu \left[\nabla \boldsymbol{v} + (\nabla \boldsymbol{v})^T\right] , \tag{2.16}$$

where $\boldsymbol{I}$ and P are an identical tensor and pressure, respectively, μ is a dynamic viscosity, and $(.)^T$ denotes tensor transposition.

Substituting Eq. (2.16) into Eq. (2.15) we get for metal and silicates, respectively,

$$\begin{aligned} \mathbf{0} &= -\nabla P^\mathrm{I} + \mu^\mathrm{I} \nabla^2 \boldsymbol{v}^\mathrm{I} , & (2.17)\\ \mathbf{0} &= -\nabla P^\mathrm{II} + \mu^\mathrm{II} \nabla^2 \boldsymbol{v}^\mathrm{II} + (\rho^\mathrm{I} - \rho^\mathrm{II})\boldsymbol{g} . & (2.18) \end{aligned}$$

It is useful to reduce Eq. (2.18) to a form similar to (2.17). Therefore we introduce an additional effective pressure Π instead of the external force satisfying $\nabla\Pi = (\rho^\mathrm{I} - \rho^\mathrm{II})\boldsymbol{g}$. In silicates thus stands

$$\mathbf{0} = -\nabla(P^\mathrm{II} - \Pi) + \mu^\mathrm{II} \nabla^2 \boldsymbol{v}^\mathrm{II} . \tag{2.19}$$

Finally, the velocities must satisfy the continuity equations

$$\begin{aligned} 0 &= \nabla \cdot \boldsymbol{v}^\mathrm{I} , & (2.20)\\ 0 &= \nabla \cdot \boldsymbol{v}^\mathrm{II} . & (2.21) \end{aligned}$$

2.4.2 Geometry

Assuming the axial symmetry of spherical coordinates, the Navier-Stokes equations have the form (differential operators in axi-symmetric spherical coordinates are listed

in Appendix A)

$$
\begin{aligned}
0 &= -\frac{\partial P^{\mathrm{I}}}{\partial r} + \mu^{\mathrm{I}}\left\{\frac{1}{r^2}\frac{\partial}{\partial r}\left(r^2\frac{\partial v_r^{\mathrm{I}}}{\partial r}\right) + \frac{1}{r^2\sin\theta}\frac{\partial}{\partial\theta}\left(\sin\theta\frac{\partial v_r^{\mathrm{I}}}{\partial\theta}\right)\right. \\
&\quad \left. -\frac{2v_r^{\mathrm{I}}}{r^2} - \frac{2}{r^2\sin\theta}\frac{\partial}{\partial\theta}\left(v_\theta^{\mathrm{I}}\sin\theta\right)\right\}, \qquad (2.22)\\
0 &= -\frac{1}{r}\frac{\partial P^{\mathrm{I}}}{\partial\theta} + \mu^{I}\left\{\frac{1}{r^2}\frac{\partial}{\partial r}\left(r^2\frac{\partial v_\theta^{\mathrm{I}}}{\partial r}\right) + \frac{1}{r^2\sin\theta}\frac{\partial}{\partial\theta}\left(\sin\theta\frac{\partial v_\theta^{\mathrm{I}}}{\partial\theta}\right)\right. \\
&\quad \left. +\frac{2}{r^2}\frac{\partial v_r^{\mathrm{I}}}{\partial\theta} - \frac{v_\theta^{\mathrm{I}}}{r^2\sin^2\theta}\right\}, \qquad (2.23)
\end{aligned}
$$

and similarly in the silicates.

The continuity equation has the form

$$
0 = \frac{1}{r^2}\frac{\partial}{\partial r}\left(r^2 v_r\right) + \frac{1}{r\sin\theta}\frac{\partial}{\partial\theta}\left(\sin\theta v_\theta\right)\,. \qquad (2.24)
$$

2.4.3 Limit and boundary conditions

We prescribe five conditions at the metal-silicate interface and one condition at infinity.

Far from the falling drop the effect of the blob is negligible and the velocity field in the silicates must approach the terminal velocity in the vertical direction $v_z = -U_{\mathrm{t}}$. In spherical coordinates

$$
\begin{aligned}
\lim_{r\to\infty} v_r^{\mathrm{II}} &= -U_{\mathrm{t}}\cos\theta\,, \qquad (2.25)\\
\lim_{r\to\infty} v_\theta^{\mathrm{II}} &= U_{\mathrm{t}}\sin\theta\,. \qquad (2.26)
\end{aligned}
$$

Since U_{t} is unknown, Eqs. (2.25)–(2.26) provide only one independent constraint.

At the interface between the drop and the surrounding liquid, $r = R$, the traction $\boldsymbol{T}$ must be continuous

$$
[\boldsymbol{T}]^+_- = [\boldsymbol{e}_r\cdot\boldsymbol{\sigma}]^+_- = 0\,, \qquad (2.27)
$$

i.e.,

$$
\begin{aligned}
[\sigma_{rr}]^+_- &= 0\,, \qquad (2.28)\\
[\sigma_{r\theta}]^+_- &= 0\,. \qquad (2.29)
\end{aligned}
$$

Because we consider a newtonian rheology (2.16) we rewrite Eqs. (2.28) and (2.29)

$$
\begin{aligned}
\left[-(P^{\mathrm{II}}-\Pi) + 2\mu^{\mathrm{II}}\frac{\partial v_r^{\mathrm{II}}}{\partial r}\right]_{r=R} &= \left[-P^{I} + 2\mu^{\mathrm{I}}\frac{\partial v_r^{\mathrm{I}}}{\partial r}\right]_{r=R}\,,\\
\mu^{\mathrm{II}}\left(\frac{1}{r}\frac{\partial v_r^{\mathrm{II}}}{\partial\theta} + \frac{\partial v_\theta^{\mathrm{II}}}{\partial r} - \frac{v_\theta^{\mathrm{II}}}{r}\right)_{r=R} &= \mu^{\mathrm{I}}\left(\frac{1}{r}\frac{\partial v_r^{\mathrm{I}}}{\partial\theta} + \frac{\partial v_\theta^{\mathrm{I}}}{\partial r} - \frac{v_\theta^{\mathrm{I}}}{r}\right)_{r=R}\,. \qquad (2.30)
\end{aligned}
$$

At the surface of the drop, normal components of velocities must be zero as no mixing occurs, and tangential velocities must satisfy that there is no-slip between the two liquids,

$$v_r^{\mathrm{I}} = 0\,|_{r=R}\,, \tag{2.31}$$
$$v_r^{\mathrm{II}} = 0\,|_{r=R}\,, \tag{2.32}$$
$$v_\theta^{\mathrm{I}} = v_\theta^{\mathrm{II}}\,|_{r=R}\,. \tag{2.33}$$

2.4.4 Solution

Boundary conditions at infinity (2.25) and (2.26) suggest to try the solution in the form

$$v_r^{\mathrm{I}} = f^{\mathrm{I}}(r)\cos\theta\,, \tag{2.34}$$
$$v_\theta^{\mathrm{I}} = g^{\mathrm{I}}(r)\sin\theta\,, \tag{2.35}$$
$$P^{\mathrm{I}} = \mu^{\mathrm{I}} h^{\mathrm{I}}(r)\cos\theta\,, \tag{2.36}$$

in the metal blob. Likewise, we write the solution in silicates

$$v_r^{\mathrm{II}} = f^{\mathrm{II}}(r)\cos\theta\,, \tag{2.37}$$
$$v_\theta^{\mathrm{II}} = g^{\mathrm{II}}(r)\sin\theta\,, \tag{2.38}$$
$$P^{\mathrm{II}} = \mu^{\mathrm{II}} h^{\mathrm{II}}(r)\cos\theta\,. \tag{2.39}$$

Substituting Eqs. (2.34)–(2.36) to Eqs. (2.22)–(2.24) and eliminating functions g and h we obtain an ordinary differential equation of the fourth order for f

$$r^3\frac{\mathrm{d}^4 f}{\mathrm{d}r^4} + 8r^2\frac{\mathrm{d}^3 f}{\mathrm{d}r^3} + 8r\frac{\mathrm{d}^2 f}{\mathrm{d}r^2} - 8\frac{\mathrm{d}f}{\mathrm{d}r} = 0\,. \tag{2.40}$$

Next, we have for the functions g and h

$$g = -\frac{1}{2r}\frac{\mathrm{d}}{\mathrm{d}r}\left(r^2 f\right)\,, \tag{2.41}$$
$$h = 2\frac{\mathrm{d}f}{\mathrm{d}r} + 3r\frac{\mathrm{d}^2 f}{\mathrm{d}r^2} + \frac{r^2}{2}\frac{\mathrm{d}^3 f}{\mathrm{d}r^3}\,. \tag{2.42}$$

The solution of Eq. (2.40) can be generally expressed in the form $f \approx r^n$ that implies through Eqs. (2.41) and (2.42) that g holds $g \approx -\frac{n+2}{2}r^n$ and similarly for h stands $h \approx \frac{1}{2}n^2(3+n)r^{n-1}$.

Substituting $f = r^n$ to Eq. (2.40) we find that n must satisfy

$$n(n-2)(n+1)(n+3) = 0\,, \tag{2.43}$$

that leads to $n = \{-3, -1, 0, 2\}$.

Considering that the velocity must remain finite at all points within the drop as well as outside, the general solution for v_r^{I}, v_θ^{I} and P^{I} is thus expressed as

$$v_r^{\mathrm{I}} = (b_1 + b_2 r^2)\cos\theta\,, \tag{2.44}$$
$$v_\theta^{\mathrm{I}} = (-b_1 - 2b_2 r^2)\sin\theta\,, \tag{2.45}$$
$$P^{\mathrm{I}} = 10\mu^{\mathrm{I}} b_2 r\cos\theta\,. \tag{2.46}$$

Similarly, it stands

$$v_r^{\mathrm{II}} = (\frac{c_1}{r^3} + \frac{c_2}{r} + c_3)\cos\theta\,, \tag{2.47}$$

$$v_\theta^{\mathrm{II}} = (\frac{c_1}{2r^3} - \frac{c_2}{2r} - c_3)\sin\theta\,, \tag{2.48}$$

$$P^{\mathrm{II}} = \mu^{\mathrm{II}}\frac{c_2}{r^2}\cos\theta\,, \tag{2.49}$$

for the solution in silicates.

Using the conditions at infinity and at the boundary we evaluate the unknown coefficients c_1, c_2, c_3, b_1, b_2 and the terminal velocity U_t obtaining the velocity field inside the blob

$$v_r^{\mathrm{I}} = \left(1 - \frac{r^2}{R^2}\right)\frac{U_\mathrm{t}\mu^{\mathrm{II}}\cos\theta}{2(\mu^{\mathrm{I}} + \mu^{\mathrm{II}})}\,, \tag{2.50}$$

$$v_\theta^{\mathrm{I}} = \left(\frac{2r^2}{R^2} - 1\right)\frac{U_\mathrm{t}\mu^{\mathrm{II}}\sin\theta}{2(\mu^{\mathrm{I}} + \mu^{\mathrm{II}})}\,, \tag{2.51}$$

the velocity field in silicates

$$v_r^{\mathrm{II}} = \left(-1 - \frac{\mu^{\mathrm{I}}}{2(\mu^{\mathrm{I}} + \mu^{\mathrm{II}})}\frac{R^3}{r^3} + \frac{3\mu^{\mathrm{I}} + 2\mu^{\mathrm{II}}}{2(\mu^{\mathrm{II}} + \mu^{\mathrm{I}})}\frac{R}{r}\right)U_\mathrm{t}\cos\theta\,, \tag{2.52}$$

$$v_\theta^{\mathrm{II}} = \left(1 - \frac{\mu^{\mathrm{I}}}{4(\mu^{\mathrm{I}} + \mu^{\mathrm{II}})}\frac{R^3}{r^3} - \frac{3\mu^{\mathrm{I}} + 2\mu^{\mathrm{II}}}{4(\mu^{\mathrm{II}} + \mu^{\mathrm{I}})}\frac{R}{r}\right)U_\mathrm{t}\sin\theta\,, \tag{2.53}$$

and finally the terminal velocity

$$U_\mathrm{t} = \frac{2(\rho^{\mathrm{II}} - \rho^{\mathrm{I}})gR^2}{3\mu^{\mathrm{II}}}\frac{\mu^{\mathrm{II}} + \mu^{\mathrm{I}}}{2\mu^{\mathrm{II}} + 3\mu^{\mathrm{I}}}\,, \tag{2.54}$$

known as the Rybczyński-Hadamard formula [1]. Figure 2.2 shows the velocity field using vectors and streamlines for one particular parameter choice.

In the solid limit, when $\mu^I \to \infty$, we get for the terminal velocity the well-known Stokes equation

$$U_\mathrm{st} = \frac{2}{9}\frac{(\rho^{\mathrm{II}} - \rho^{\mathrm{I}})gR^2}{\mu^{\mathrm{II}}}\,. \tag{2.55}$$

The velocity field outside the solid drop with no-slip boundary condition at the solid-liquid interface is then [26]

$$v_r^{\mathrm{II}} = \left(-1 - \frac{R^3}{2r^3} + \frac{3R}{2r}\right)U_\mathrm{st}\cos\theta\,, \tag{2.56}$$

$$v_\theta^{\mathrm{II}} = \left(1 - \frac{R^3}{4r^3} - \frac{3R}{4r}\right)U_\mathrm{st}\sin\theta\,. \tag{2.57}$$

Comparing the Rybczyński-Hadamard terminal velocity for a liquid drop in a liquid medium with the Stokes terminal velocity for a solid drop in a liquid medium, we see that the steady state fall of a liquid sphere is faster than that of a solid one in the same gravity field. Figure 2.3 shows the ratio of the R-H velocity and the Stokes velocity $\mathcal{R}_\mathrm{U} = U_\mathrm{t}/U_\mathrm{st}$ as a function of the silicate viscosity for two different iron viscosities.

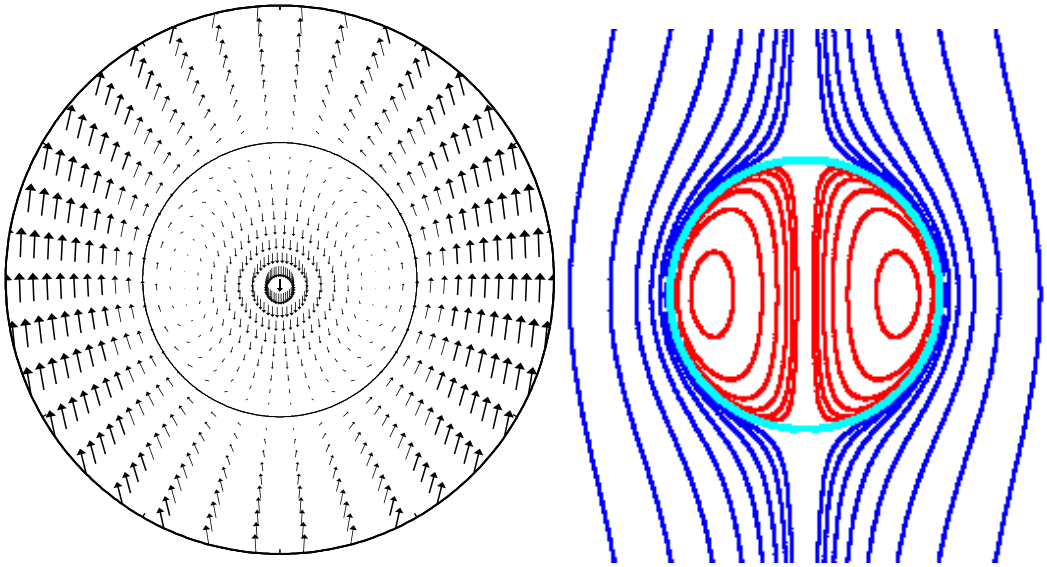

(a) Velocity field (b) Streamlines

Figure 2.2: Velocity field and streamlines for steady state motion of liquid blob in liquid medium in viscous regime. Used parameters are: $R = 1\,\mathrm{m}$, $U_\mathrm{t} = 1\,\mathrm{m/s}$ and viscosities $\mu^\mathrm{I} = \mu^\mathrm{II} = 1\,\mathrm{Pa\,s}$.

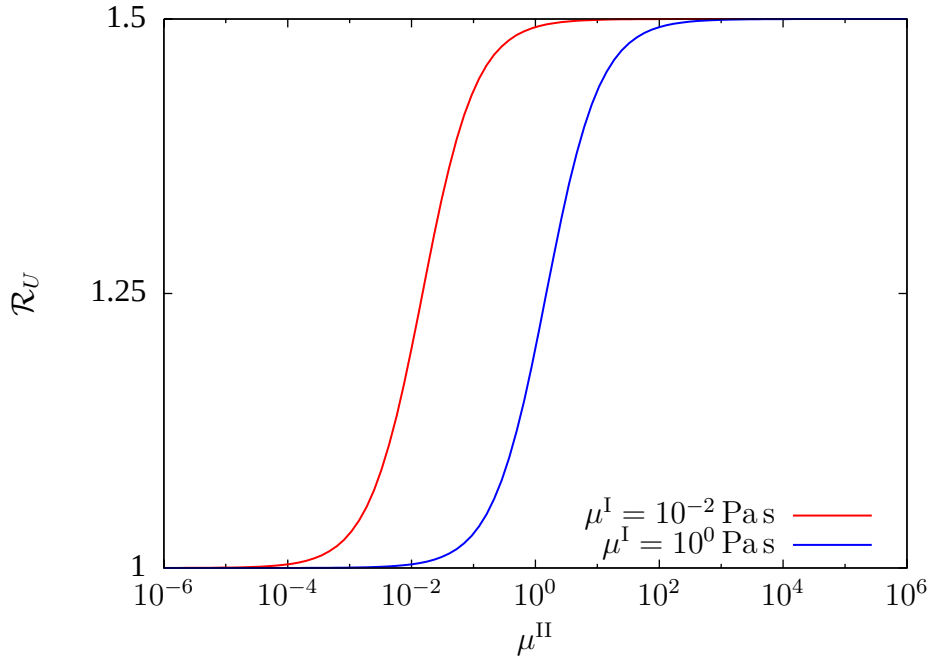

Figure 2.3: Ratio of terminal velocities $\mathcal{R}_U$ for liquid and solid sphere in a liquid medium as a function of silicate viscosity μ^II for two different iron viscosities μ^I.

2.5 Dimensionless formulation

To reduce the number of parameters that characterize the system it is convenient to use dimensionless variables. We introduce three scaling factors: the radius of the blob R for r, the terminal velocity U_t for $\boldsymbol{v}$ and the reference concentration C_0 for C. As a reference concentration we use the initial concentration. Time is scaled with advective factor R/U_t. Equations (2.7) and (2.8) thus become

$$\frac{\partial C^{\mathrm{I}*}}{\partial t^*} = \nabla^* \cdot \left(\frac{D^{\mathrm{I}}}{D^{\mathrm{II}}} \frac{1}{\mathrm{Pe}} \nabla C^{\mathrm{I}*} - \boldsymbol{v}^{\mathrm{I}*} C^{\mathrm{I}*} \right) , \tag{2.58}$$

$$\frac{\partial C^{\mathrm{II}*}}{\partial t^*} = \nabla^* \cdot \left(\frac{1}{\mathrm{Pe}} \nabla C^{\mathrm{II}*} - \boldsymbol{v}^{\mathrm{II}*} C^{\mathrm{II}*} \right) , \tag{2.59}$$

where index $(.)^*$ denotes the non-dimensional variables. We introduced the Peclet number

$$\mathrm{Pe} = \frac{R U_\mathrm{t}}{D^{\mathrm{II}}} , \tag{2.60}$$

that relates the rate of advection to the rate of chemical diffusion in the silicates.

Since the non-dimensional velocity depends on the ratio of viscosities, the system is scaled by three dimensionless numbers, namely the ratio of diffusion coefficients $\mathcal{R}_D = D^{\mathrm{I}}/D^{\mathrm{II}}$, the ratio of viscosities $\mathcal{R}_\mu = \mu^{\mathrm{I}}/\mu^{\mathrm{II}}$ and the Peclet number Pe.

From now on, we work with the dimensionless quantities and omit the asterisk.

2.6 Analytical model

In order to find an analytical model that could be compared with the results of numerical code established below in Chapter 3 we evaluate the mean value of convective-diffusion equation (2.58) within the drop

$$\left\langle \frac{\partial C^{\mathrm{I}}}{\partial t} \right\rangle = \left\langle \nabla \cdot \left(\frac{\mathcal{R}_\mathrm{D}}{\mathrm{Pe}} \nabla C^{\mathrm{I}} - \boldsymbol{v}^{\mathrm{I}} C^{\mathrm{I}} \right) \right\rangle , \tag{2.61}$$

that leads with use of the divergence theorem to equation

$$\frac{\partial \langle C^{\mathrm{I}} \rangle}{\partial t} = \frac{\int_S \frac{\mathcal{R}_\mathrm{D}}{\mathrm{Pe}} \nabla C^{\mathrm{I}} \, \mathrm{d}\boldsymbol{S}}{V} , \tag{2.62}$$

where we exchanged the time derivation and the volume integral. Here, S is the surface of the drop and $V = \frac{4}{3}\pi$ is its dimensionless volume. We considered that the radial part of the advective flux is zero over the surface (2.31).

Further, we allow for no concentration accumulation on the boundary (2.9), i.e.,

$$\int_S \frac{\mathcal{R}_\mathrm{D}}{\mathrm{Pe}} \nabla C^{\mathrm{I}} \, \mathrm{d}\boldsymbol{S} = \int_S \frac{1}{\mathrm{Pe}} \nabla C^{\mathrm{II}} \, \mathrm{d}\boldsymbol{S} , \tag{2.63}$$

and will search for analytical representation of the surface integral for the concentration outside the drop.

There are only few cases when the exact solution of the surface integral (2.63) can be obtained. Here, we present an approximative solution considering the boundary layer equation for steady convective motion.

The equation of steady convection mass transfer in the diffusion boundary layer follows

$$\boldsymbol{v}_r^{\mathrm{II}}\frac{\partial C^{\mathrm{II}}}{\partial r}+\frac{\boldsymbol{v}_\theta^{\mathrm{II}}}{r}\frac{\partial C^{\mathrm{II}}}{\partial \theta}=\frac{1}{\mathrm{Pe}}\left(\frac{\partial^2 C^{\mathrm{II}}}{\partial r^2}+\frac{2}{r}\frac{\partial C^{\mathrm{II}}}{\partial r}\right), \tag{2.64}$$

where we omitted the angular part of the Laplacian on the right hand side because the derivatives along the surface of the sphere are small compared to the derivatives along the radius vector.

In order to solve Eq. (2.64), boundary conditions must be established. Since the change of concentration occurs in a thin layer near the drop surface, the condition on constant concentration C_1 far from the surface is taken (2.65). Next, at the surface of the body, we impose the constant concentration C_2 that can generally vary with time (2.66). Boundary conditions are thus

$$C^{\mathrm{II}} = C_1\,|_{r\to\infty}\,, \tag{2.65}$$
$$C^{\mathrm{II}} = C_2\,|_{r=1}\,. \tag{2.66}$$

In order to integrate Eq. (2.64) we introduce the stream function Ψ, related to $\boldsymbol{v}_r^{\mathrm{II}}$ and $\boldsymbol{v}_\theta^{\mathrm{II}}$ as follows

$$\boldsymbol{v}_r^{\mathrm{II}} = -\frac{1}{r^2\sin\theta}\frac{\partial\Psi}{\partial\theta}\,, \tag{2.67}$$

$$\boldsymbol{v}_\theta^{\mathrm{II}} = \frac{1}{r\sin\theta}\frac{\partial\Psi}{\partial r}\,. \tag{2.68}$$

Because we are interested in solutions only near the surface, we further introduce a new variable y

$$y = r-1\,, \tag{2.69}$$

being the distance from the surface $r=1$.

Let us evaluate the order of magnitude of the concentration derivatives in the boundary layer. For small y, i.e. $y\sim\delta\ll 1$, we have

$$\frac{\partial^2 C^{\mathrm{II}}}{\partial y^2} \sim \frac{C^{\mathrm{II}}}{\delta^2}\,, \tag{2.70}$$
$$\frac{\partial C^{\mathrm{II}}}{\partial y} \sim \frac{C^{\mathrm{II}}}{\delta}\,, \tag{2.71}$$

and therefore

$$\frac{\partial^2 C^{\mathrm{II}}}{\partial y^2} \gg 2\frac{\partial C^{\mathrm{II}}}{\partial y}\,. \tag{2.72}$$

Under these assumptions and by replacing (y,θ) with new variables (Ψ,θ) we solve Eq. (2.64),

$$\frac{\partial C^{\mathrm{II}}}{\partial\theta}=\frac{1}{\mathrm{Pe}}\sin\theta\frac{\partial}{\partial\Psi}\left[\sin\theta\boldsymbol{v}_\theta^{\mathrm{II}}\frac{\partial C^{\mathrm{II}}}{\partial\Psi}\right]. \tag{2.73}$$

Next, one more condition must be given along with (2.65) and (2.66) since the stream function is determined up to an arbitrary constant. We require that the concentration $C(\Psi, \theta)$ has no singularity at the point of incidence of the flow on the sphere, i.e.,

$$C^{\mathrm{II}} = C_1 \mid_{\theta=0\,,\Psi=0} \,. \tag{2.74}$$

Last of all, we allow for the tangential velocity at values $y = 0$, i.e.,

$$v_\theta \mid_{y=0} = \frac{\mu^{\mathrm{II}}}{2(\mu^I + \mu^{II})} \sin\theta \,. \tag{2.75}$$

The solution of equation (2.73) can be found in [11] complete with the evaluation of the surface integral (2.63). We present here only the final result of the total flow over the surface without its derivation. The total flow I_{liq} for the liquid sphere is then

$$I_{\mathrm{liq}} = 8\sqrt{\frac{\pi}{6}\frac{\mu^{\mathrm{II}}}{\mu^{\mathrm{I}} + \mu^{\mathrm{II}}}}(C_1 - C_2)\sqrt{\frac{1}{\mathrm{Pe}}} \,. \tag{2.76}$$

Next, we match the concentration at the surface of the drop C_2 with the average concentration within the drop as

$$C_2 = \frac{\langle C^{\mathrm{I}} \rangle}{K} \,, \tag{2.77}$$

where we allow for the concentration discontinuity at the surface given by Eq. (2.10) produced by different partitioning of the elements. It is properly as far as the diffusion within the drop is sufficiently high or the mixing within the drop is sufficient in order to rapidly homogenize the concentration.

Using the evaluation of the total flux over the surface (2.76), with the average concentration as a boundary condition, we integrate Eq. (2.62) by way of variable separation getting

$$\langle C^{\mathrm{I}} \rangle = (1 - KC_1) \exp\left(-\sqrt{\frac{6}{\pi}\frac{\mu^{\mathrm{II}}}{\mu^{\mathrm{I}} + \mu^{\mathrm{II}}}}\frac{1}{K}\frac{1}{\sqrt{\mathrm{Pe}}}t \right) + KC_1 \,, \tag{2.78}$$

where t and $\langle C^{\mathrm{I}} \rangle$ are dimensionless time and concentration, respectively.

For the time evolution of the mean concentration thus stands an exponential law

$$\langle C^{\mathrm{I}} \rangle \sim \exp\left(-\frac{t}{\tau} \right) \,, \tag{2.79}$$

where we introduced a characteristic time τ satisfying

$$\tau_{\mathrm{liq}} = \sqrt{\frac{\pi}{6}\left(\frac{\mu^{\mathrm{I}}}{\mu^{\mathrm{II}}} + 1 \right)} K\sqrt{\mathrm{Pe}} \,. \tag{2.80}$$

We can proceed the same derivation for the rigid sphere in addition to the angular velocity that is always zero at the surface. We thus express the tangential velocity $\boldsymbol{v}_\theta^{\mathrm{II}}$ near the surface.

The total flow I_{rig} to the surface of the drop is then

$$I_{\mathrm{rig}} = 7.98(C_1 - C_2)(\mathrm{Pe})^{-2/3}\,, \tag{2.81}$$

where the factor of 7.98 comes from the integration constant. Using (2.81) the time evolution of concentration is

$$\langle C^{\mathrm{I}} \rangle = (1 - KC_1) \exp\left(-\frac{5.985}{\pi}\frac{1}{K}\,(\mathrm{Pe})^{-\frac{2}{3}}\,t\right) + KC_1\,, \tag{2.82}$$

with the characteristic time

$$\tau_{\mathrm{rig}} = \frac{\pi}{5.985} K (\mathrm{Pe})^{\frac{2}{3}}\,. \tag{2.83}$$

2.7 Parameters of the model

In a liquid medium, dispersed small particles tend to grow in order to reduce the surface energy. On the other hand, large objects are subjected to repeated breakups till they settle down. The important question is thus the extent of these two mechanisms that lead to establish the drops in a state when surface tension prevents further breakup and when surface energy reaches minimum.

The crucial forces in a moving liquid-liquid system are the inertia and the surface tension forces. The dimensionless number that reflects their ratio is the Weber number given as [15]

$$\mathrm{We} = \frac{2\rho^{\mathrm{II}} R U_{\mathrm{t}}^2}{\gamma}\,. \tag{2.84}$$

The smaller the Weber number, the more stable the drop is. The basic question is what is the critical radius when the drop is still stable.

Considering the Kelvin-Helmholtz instability that is a consequence of shear motion between two liquids at the interface, it is possible to constrain the stable size of droplet. Using numerical computing and theoretical investigation, the critical Weber number $\mathrm{We}_{\mathrm{cr}}$ reflecting the instabilities is determined as [8]

$$\mathrm{We}_{\mathrm{cr}} = 4\pi(1 + \frac{1}{s})\,, \tag{2.85}$$

where $s = \frac{\rho^{\mathrm{I}}}{\rho^{\mathrm{II}}}$. It is thus the ratio of densities that we consider to establish the stable radius of the drop. Using silicate and iron densities, $\rho^{\mathrm{I}} = 7800\,\mathrm{kg\,m^{-3}}$ and $\rho^{\mathrm{II}} = 3750\,\mathrm{kg\,m^{-3}}$, the critical Weber number is $\mathrm{We}_{\mathrm{cr}} = 19$.

Equating the definition of Weber number (2.84) with the critical Weber number (2.85) and using an analytical solution for the terminal velocity (2.54) stable radius R_s of the drop is

$$R_{\mathrm{s}} = \sqrt[5]{\frac{\pi\gamma(1+\frac{1}{s})}{2\rho^{\mathrm{II}}}\left(\frac{3\mu^{\mathrm{II}}}{(\rho^{\mathrm{II}} - \rho^{\mathrm{I}})g}\frac{2\mu^{\mathrm{II}} + 3\mu^{\mathrm{I}}}{\mu^{\mathrm{II}} + \mu^{\mathrm{I}}}\right)^2}\,. \tag{2.86}$$

Figure 2.4 shows the stable size of drops, the terminal velocity, and the Peclet number as functions of silicate viscosity varying in a range of $10^{-6} - 10^{6}\,\mathrm{Pa\,s}$ (assuming $\gamma = 1\,\mathrm{Nm}^{-1}$ and $g = 10\,\mathrm{ms}^{-2}$). The stable size of the drop and the terminal velocity are displayed for two iron viscosities.

The stable radius varies from $\sim 10\,\mu\mathrm{m}$ for silicate viscosity $10^{-6}\,\mathrm{Pa\,s}$ to $\sim 1\,\mathrm{m}$ for silicate viscosity $10^{6}\,\mathrm{Pa\,s}$. Corresponding settling velocity varies in a range of $\sim 1\,\mathrm{cm/s} - 10\,\mathrm{m/s}$ (which could be $10\times$ smaller due to the vigorous convection of the magma ocean [2]). The higher the silicate viscosity, the larger the stable radius and the slower the terminal velocity.

The Peclet number varies in a range of $10^{4} - 10^{11}$ for diffusion coefficient $10^{-8} - 10^{-12}\,\mathrm{m^2/s}$. For one diffusion coefficient Peclet number changes about two orders within the viscosity range. The higher the viscosity, the higher the Peclet number and thus the more significant the advection is with respect to the diffusion.

Figure 2.5 shows the ratio of average velocities within the drop and outside $\mathcal{R}_{\langle \mathrm{v} \rangle} = \langle v^{\mathrm{I}} \rangle / \langle v^{\mathrm{II}} \rangle$ as a function of the ratio of viscosities $\mathcal{R}_{\mu}$ for the stable size of the drop (cp. with Figure 2.3).

The velocity ratio remains nearly constant when the silicate viscosity is higher than the viscosity of iron. On the other hand, for the iron viscosity higher than the silicate viscosity stirring within the blob starts to be less efficient and the velocity ratio decreases rapidly.

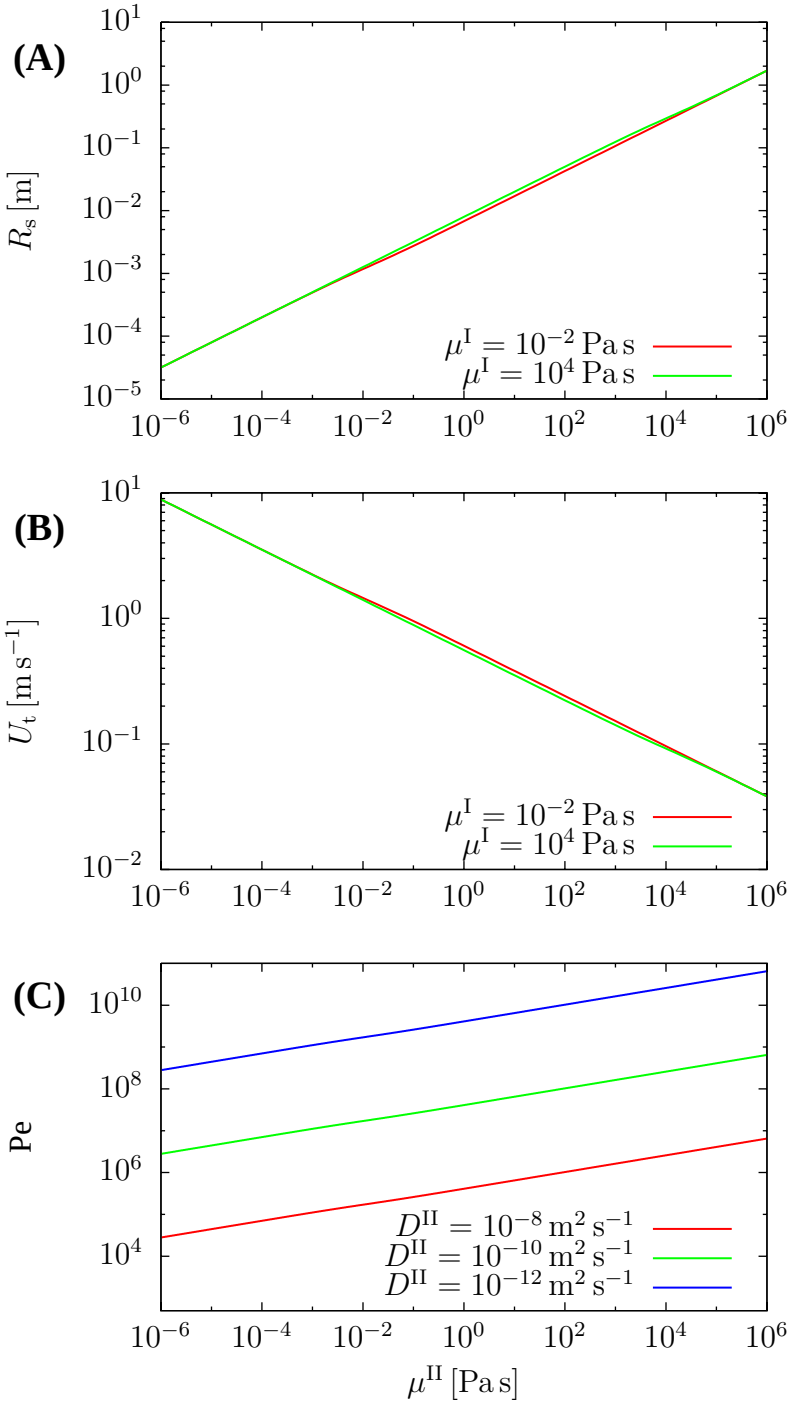

Figure 2.4: (A) Stable radius of the drop R_s and (B) terminal velocity U_t as a function of silicate viscosity for two different iron viscosities. Stable droplet size is estimated using the critical Weber number $We_{cr} = 19$. (C) Peclet number Pe as a function of silicate viscosity for three different diffusion coefficients. Peclet number is computed for stable size of the drop and corresponding terminal velocity.

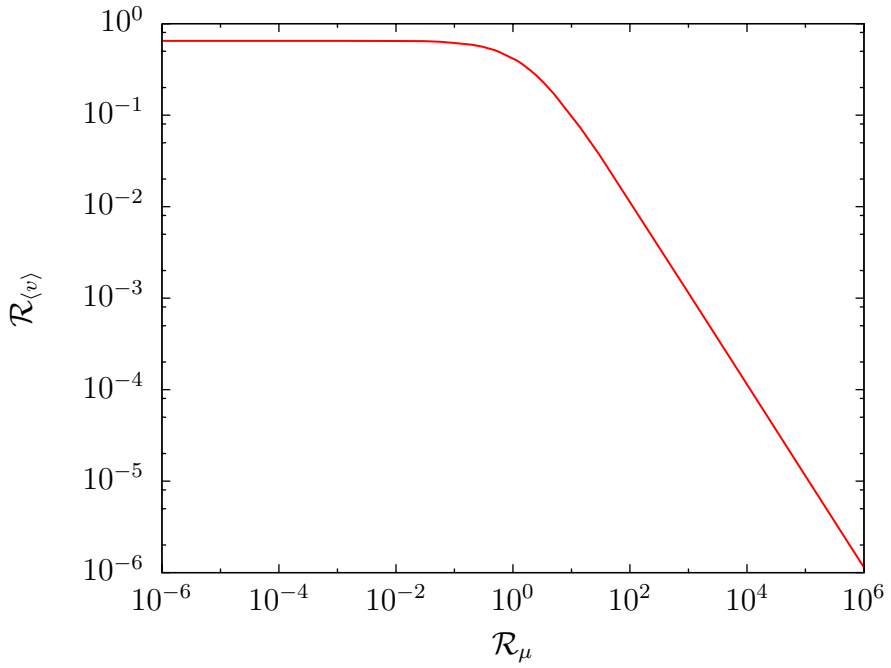

Figure 2.5: Ratio of average velocities within the blob and outside $\mathcal{R}_{\langle \mathrm{v} \rangle}$ as a function of viscosity ratio $\mathcal{R}_\mu$. Calculations are done for stable size of the drop.

Chapter 3

Numerical Model

To solve the flux conservative equations (2.7) and (2.8) with the boundary conditions (2.10)-(2.12) and a velocity field governed by Eq. (2.50)-(2.53), we use a finite volume formulation in spatial domain and an alternating direction implicit (ADI) method in time domain. Both of them are of the second order accuracy.

3.1 Finite volume formulation

Generally, in the finite volume method [27] a partial differential equation is integrated over the volume of an element. The divergence term is then converted using the divergence theorem to a surface integral. Then the balance of in-flux and out-flux through the faces of the element is prescribed. As the flux entering the grid element must be the same as that leaving the element, we are talking about a conservative method.

Given the discretization in the radial direction and the lateral direction, $r_j = (j-1)\Delta r$, $j = 1, \ldots, JMAX$, $\theta_k = (k-1)\Delta\theta$, $k = 1, \ldots, KMAX$, respectively, we evaluate vectors at points $(r_j + \frac{1}{2}\Delta r, \theta_k)$ and $(r_j, \theta_k + \frac{1}{2}\Delta\theta)$, where Δr and $\Delta\theta$ denote the grid spacings. $JMAX,\ KMAX \in \mathbb{N}$ are natural numbers. Scalar variables are considered piecewise constant over the mesh cells at each time step. They are represented by their values at discrete points $(r_j + \frac{1}{2}\Delta r, \theta_k + \frac{1}{2}\Delta\theta)$. Taking into account the discretization, we refer further to $C(r_j + \frac{1}{2}\Delta r, \theta_k + \frac{1}{2}\Delta\theta)$ as $C_{j,k}$ (likewise for other variables), $j = 1, \ldots, JMAX$, $k = 1, \ldots, KMAX$.

Our aim is to solve Eqs. (2.58) and (2.59). Because these equations are formally the same, we proceed a numerical analysis with general concentration C, vector field $\boldsymbol{v}$ and dimensionless constant $\mathcal{D}$ beeing either $\mathcal{R}_{\mathrm{D}}/\mathrm{Pe}$ in the domain I or $1/\mathrm{Pe}$ in the domain II.

Applying approach described above we get

$$\iiint_{\Omega} \frac{\partial C}{\partial t} \mathrm{d}V = -\iint_{\partial\Omega} \boldsymbol{F} \cdot \boldsymbol{n} \mathrm{d}S\,, \tag{3.1}$$

where Ω is the finite volume, $\partial\Omega$ is the boundary of the finite volume and $\boldsymbol{n}$ is an outer normal to the surface element.

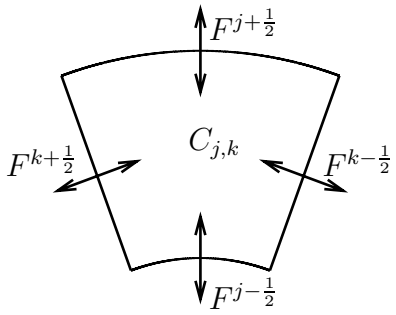

Figure 3.1: Balance of in-flux and out-flux across surface of an inner element in the 2-D spherical grid. Concentration $C_{j,k}$ is computed at the center of the cell. Fluxes are calculated at the faces of the cell ; radial flux on the vertical faces and tangential flux on the horizontal faces.

Now, we balance the in-flux and the out-flux in each cell. We introduce the flux across faces of the cell in the grid: $F^{j+\frac{1}{2}}$, $F^{j-\frac{1}{2}}$, $F^{k+\frac{1}{2}}$, $F^{k-\frac{1}{2}}$, cf. Figure 3.1. Similarly, we write for particular surface elements of the cell's faces $S^{j+\frac{1}{2}}$, $S^{j-\frac{1}{2}}$, $S^{k+\frac{1}{2}}$, $S^{k-\frac{1}{2}}$.

Then we evaluate integrals of the normal components of the flux across borders of the cell and the volume integral in (3.1)

$$\frac{\partial C_{j,k}}{\partial t} = -\frac{F^{k+\frac{1}{2}}S^{k+\frac{1}{2}} - F^{k-\frac{1}{2}}S^{k-\frac{1}{2}}}{V_{j,k}} - \frac{F^{j+\frac{1}{2}}S^{j+\frac{1}{2}} - F^{j-\frac{1}{2}}S^{j-\frac{1}{2}}}{V_{j,k}}\,, \tag{3.2}$$

where $V_{j,k}$ is the element's volume. The right hand side (RHS) is thus separated to radial and angular part.

As we described in Chapter 2 we use an axi-symmetrical spherical coordinates with the origin at the center of the drop. For volume element thus stands

$$\begin{aligned} V_{j,k} &= \int_0^{2\pi}\int_{r_j}^{r_j+\Delta r}\int_{\theta_k}^{\theta_k+\Delta\theta} r^2\sin\theta\,\mathrm{d}r\,\mathrm{d}\phi\,\mathrm{d}\theta \\ &= \frac{2}{3}\pi(\cos\theta_k - \cos(\theta_k+\Delta\theta))[(r_j+\Delta r)^3 - r_j^3]\,. \end{aligned} \tag{3.3}$$

The surface elements are expressed as follows,

$$\begin{aligned} S^{j+\frac{1}{2}} &= \int_0^{2\pi}\int_{\theta_k}^{\theta_k+\Delta\theta} (r_j+\Delta r)^2\sin\theta\,\mathrm{d}\theta\,\mathrm{d}\phi \\ &= 2\pi(r_j+\Delta r)^2(\cos\theta_k - \cos(\theta_k+\Delta\theta))\,, \end{aligned} \tag{3.4}$$

$$\begin{aligned} S^{j-\frac{1}{2}} &= \int_0^{2\pi}\int_{\theta_k}^{\theta_k+\Delta\theta} r_j^2\sin\theta\,\mathrm{d}\theta\,\mathrm{d}\phi \\ &= 2\pi r_j^2(\cos\theta_k - \cos(\theta_k+\Delta\theta))\,, \end{aligned} \tag{3.5}$$

$$
\begin{aligned}
S^{k+\frac{1}{2}} &= \int_0^{2\pi}\int_{r_j}^{r_j+\Delta r} r\sin\theta_k \,\mathrm{d}r\,\mathrm{d}\phi \\
&= \pi\sin\theta_k(2r_j dr + \Delta r^2)\,, \qquad (3.6)\\
S^{k-\frac{1}{2}} &= \int_0^{2\pi}\int_{r_j}^{r_j+\Delta r} r\sin(\theta_k + d\theta)\,\mathrm{d}r\,\mathrm{d}\phi \\
&= \pi\sin(\theta_k+\Delta\theta)(2r_j\Delta r + \Delta r^2)\,. \qquad (3.7)
\end{aligned}
$$

Changes of concentration can proceed by microscopic diffusion or macroscopic advection flux as described in Chapter 2. Thus, we can write for the flux across a surface element

$$
\begin{aligned}
F^{j\pm\frac{1}{2}} &= -\mathcal{D}\left(\frac{\partial C}{\partial r}\right)^{j\pm\frac{1}{2}} + v_r C^{j\pm\frac{1}{2}}\,, \qquad (3.8)\\
F^{k\pm\frac{1}{2}} &= -\frac{\mathcal{D}}{r}\left(\frac{\partial C}{\partial \theta}\right)^{k\pm\frac{1}{2}} + v_\theta C^{k\pm\frac{1}{2}}\,, \qquad (3.9)
\end{aligned}
$$

where concentration and derivatives of concentration are expressed at the faces of the cell in the grid as is denoted by indices $j\pm\frac{1}{2}\,, k\pm\frac{1}{2}$.

The finite volume method provides high spatial accuracy depending upon which discretization we use. As we suppose that we don't handle with shocks or sharp discontinuities, we assume a central discretization for concentration and central difference scheme for derivatives that are of second order spatial accuracy,

$$
\begin{aligned}
C^{k+\frac{1}{2}} &= \tfrac{C_{j,k}+C_{j,k+1}}{2}\,, & C^{k-\frac{1}{2}} &= \tfrac{C_{j,k}+C_{j,k-1}}{2}\,,\\
C^{j+\frac{1}{2}} &= \tfrac{C_{j,k}+C_{j+1,k}}{2}\,, & C^{j-\frac{1}{2}} &= \tfrac{C_{j,k}+C_{j-1,k}}{2}\,,
\end{aligned} \qquad (3.10)
$$

$$
\begin{aligned}
(\partial_\theta C)^{k+\frac{1}{2}} &= \tfrac{C_{j,k+1}-C_{j,k}}{\Delta\theta}\,, & (\partial_\theta C)^{k-\frac{1}{2}} &= \tfrac{C_{j,k}-C_{j,k-1}}{\Delta\theta}\,,\\
(\partial_r C)^{j+\frac{1}{2}} &= \tfrac{C_{j+1,k}-C_{j,k}}{\Delta r}\,, & (\partial_r C)^{j-\frac{1}{2}} &= \tfrac{C_{j,k}-C_{j-1,k}}{\Delta r}\,.
\end{aligned} \qquad (3.11)
$$

Although central difference scheme provides great accuracy for smooth solutions it is not total variation diminishing (TVD) scheme, i.e. $\sum_{j,k}|C^{n+1}_{j+1,k+1} - C^{n+1}_{j,k}| \leq \sum_{j,k}|C^{n}_{j+1,k+1} - C^{n}_{j,k}|$ doesn't hold for each time step (time stepping is denoted by the superscript n), and could introduce oscillations. In that case it is appropriate to use limiter functions, e.g. superbee, that limit the slope of the piecewise approximations to avoid spurious oscillations. However, it is out of the scope of the thesis to use any of these schemes.

After introducing needed discretization, we can write for the angular and radial part of the RHS of Eq. (3.2), respectively,

$$\begin{aligned}(\mathrm{RHS})_\theta &= \frac{S^{k+\frac{1}{2}}\mathcal{D}\frac{C_{j,k+1}-C_{j,k}}{(r_j+\frac{1}{2}\Delta r)\Delta\theta} - S^{k-\frac{1}{2}}\mathcal{D}\frac{C_{j,k}-C_{j,k-1}}{(r_j+\frac{1}{2}\Delta r)\Delta\theta}}{V_{j,k}} \\ &- \frac{S^{k+\frac{1}{2}}v_\theta\frac{C_{j,k}+C_{j,k+1}}{2} - S^{k-\frac{1}{2}}v_\theta\frac{C_{j,k}+C_{j,k-1}}{2}}{V_{j,k}}\,, \qquad (3.12)\\ (\mathrm{RHS})_r &= \frac{S^{j+\frac{1}{2}}\mathcal{D}\frac{C_{j+1,k}-C_{j,k}}{\Delta r} - S^{j-\frac{1}{2}}\mathcal{D}\frac{C_{j,k}-C_{j-1,k}}{\Delta r}}{V_{j,k}} \\ &- \frac{S^{j+\frac{1}{2}}v_r\frac{C_{j,k}+C_{j+1,k}}{2} - S^{j-\frac{1}{2}}v_r\frac{C_{j,k}+C_{j-1,k}}{2}}{V_{j,k}}\,. \qquad (3.13)\end{aligned}$$

3.2 Time-integration scheme

For time strategy we consider the alternating direction implicit method. The method is based on the Crank-Nicolson scheme that we derive in the next section.

3.2.1 Crank-Nicolson Scheme

We want to find solution of $\partial_t C = g$, where ∂_t denotes a time derivation. Using Taylor series

$$C(t+\Delta t) = C(t) + \frac{\partial C}{\partial t}\Delta t + \frac{\Delta t^2}{2}\frac{\partial^2 C}{\partial t^2} + \mathcal{O}(\Delta t^3)\,, \qquad (3.14)$$

and substituting for $\partial_t C$ we get

$$C(t+\Delta t) = C(t) + g\Delta t + \frac{\Delta t^2}{2}\frac{\partial g}{\partial t} + \mathcal{O}(\Delta t^3)\,. \qquad (3.15)$$

Using Taylor series for g

$$\frac{\partial g}{\partial t} = \frac{g(t+\Delta t) - g(t)}{\Delta t} + \mathcal{O}(\Delta t)\,, \qquad (3.16)$$

the Crank-Nicolson scheme [5] is obtained,

$$\frac{C(t+\Delta t) - C(t)}{\Delta t} = \frac{1}{2}\left(g(t+\Delta t) + g(t)\right) + \mathcal{O}(\Delta t^2)\,. \qquad (3.17)$$

The scheme is of the second order accuracy.

3.2.2 ADI

Further, we introduce the alternating direction implicit method (ADI) based on the Crank-Nicolson scheme derived above with a special form of right hand side $\partial_t C =$

ΛC, where Λ is a sum of linear differential operators. More precisely, for an axisymmetrical problem in spherical coordinates stands $\Lambda = \Lambda_\theta + \Lambda_r$. We write thus

$$(1 - \frac{\Delta t}{2}\Lambda_\theta - \frac{\Delta t}{2}\Lambda_r)C^{n+1} = (1 + \frac{\Delta t}{2}\Lambda_\theta + \frac{\Delta t}{2}\Lambda_r)C^n + \mathcal{O}(\Delta t^3)\,, \tag{3.18}$$

where C^n denotes a concentration in time t_n, where $n = 1, \ldots, N$; $N \in \mathbb{N}$ (spatial indexing is omitted here).

By adding operator $\frac{\Delta t^2}{4}\Lambda_\theta\Lambda_r$ we rewrite (3.18)

$$(1 - \frac{\Delta t}{2}\Lambda_\theta)(1 - \frac{\Delta t}{2}\Lambda_r)C^{n+1} = (1 + \frac{\Delta t}{2}\Lambda_\theta)(1 + \frac{\Delta t}{2}\Lambda_r)C^n + \mathcal{O}(\Delta t^3)\,, \tag{3.19}$$

since $\frac{\Delta t^2}{4}\Lambda_\theta\Lambda_r\,(C^{n+1} - C^n)$ is included in error $\mathcal{O}(\Delta t^3)$.

Finally, we use the Peaceman-Rachford scheme, cf. [7] and [16], to solve (3.19)

$$\begin{aligned}(1 - \frac{\Delta t}{2}\Lambda_r)C^{n+\frac{1}{2}} &= (1 + \frac{\Delta t}{2}\Lambda_\theta)C^n\,,\\ (1 - \frac{\Delta t}{2}\Lambda_\theta)C^{n+1} &= (1 + \frac{\Delta t}{2}\Lambda_r)C^{n+\frac{1}{2}}\,.\end{aligned} \tag{3.20}$$

The scheme thus involves two distinct steps to gain solution at time $t_{n+1} = (n + 1)\Delta t$ from the known solution at time $t_n = n\Delta t$. Obtaining the concentration at time $t_{n+1/2} = (n+\frac{1}{2})\Delta t$ is solely of numerical nature and can be considered as an auxiliary solution without any physical meaning.

Considering that at each time step hold in spatial domain Eq. (3.12) and (3.13), respectively, we write for $(1 - \frac{\Delta t}{2}\Lambda_r)C_{j,k}^{n+\frac{1}{2}}$

$$\begin{aligned}&-\frac{S^{j-\frac{1}{2}}\Delta t}{2V_{j,k}}\left(\frac{\mathcal{D}}{\Delta r} + \frac{v_r}{2}\right)C_{j-1,k}^{n+\frac{1}{2}} \quad +\\ &\left\{1 + \frac{\Delta t}{2V_{j,k}}\left(\frac{\mathcal{D}(S^{j+\frac{1}{2}} + S^{j-\frac{1}{2}})}{\Delta r} + \frac{S^{j+\frac{1}{2}}v_r - S^{j-\frac{1}{2}}v_r}{2}\right)\right\}C_{j,k}^{n+\frac{1}{2}} \quad +\\ &-\frac{S^{j+\frac{1}{2}}\Delta t}{2V_{j,k}}\left(\frac{\mathcal{D}}{\Delta r} - \frac{v_r}{2}\right)C_{j+1,k}^{n+\frac{1}{2}}\,.\end{aligned} \tag{3.21}$$

Likewise, it stands for the angular part $(1 - \frac{\Delta t}{2}\Lambda_\theta)C_{j,k}^{n+1}$,

$$\begin{aligned}&-\frac{S^{k+\frac{1}{2}}\Delta t}{2V_{j,k}}\left(\frac{\mathcal{D}}{(r_j + \frac{1}{2}\Delta r)\Delta\theta} + \frac{v_\theta}{2}\right)C_{j,k-1}^{n+1} \quad +\\ &\left\{1 + \frac{\Delta t}{2V_{j,k}}\left(\frac{\mathcal{D}(S^{k-\frac{1}{2}} + S^{k+\frac{1}{2}})}{(r_j + \frac{1}{2}\Delta r)\Delta\theta} + \frac{S^{k-\frac{1}{2}}v_\theta - S^{k+\frac{1}{2}}v_\theta}{2}\right)\right\}C_{j,k}^{n+1} \quad +\\ &-\frac{S^{k-\frac{1}{2}}\Delta t}{2V_{j,k}}\left(\frac{\mathcal{D}}{(r_j + \frac{1}{2}\Delta r)\Delta\theta} - \frac{v_\theta}{2}\right)C_{j,k+1}^{n+1}\,.\end{aligned} \tag{3.22}$$

To calculate the concentration $C_{j,k}$ in the grid cell at time $t_{n+1/2}$ we thus need the concentration in two vertical adjoining cells $C_{j+1,k}$ and $C_{j-1,k}$. Likewise, to compute concentration $C_{j,k}$ in the grid cell at time t_n we need concentration in two horizontal adjoining cells $C_{j,k+1}$ and $C_{j,k-1}$. The demi-steps are thus decoupled to radial and angular part.

Considering all points in the mesh, a tridiagonal matrix is set up. Finally, we use subroutine `TRIDIAG` [17] to solve the equation system (3.20).

3.3 Discretization of the boundary conditions

When we want to evaluate the concentration next to the boundary, a grid cell outside the domain is involved. We call such cells "imaginary cells" and denote the corresponding C by an asterisk. Figure 3.3 shows imaginary cells within inner, outer and external part of the computational domain. In the next subsections we evaluate the concentration in the imaginary cells in terms of the boundary conditions.

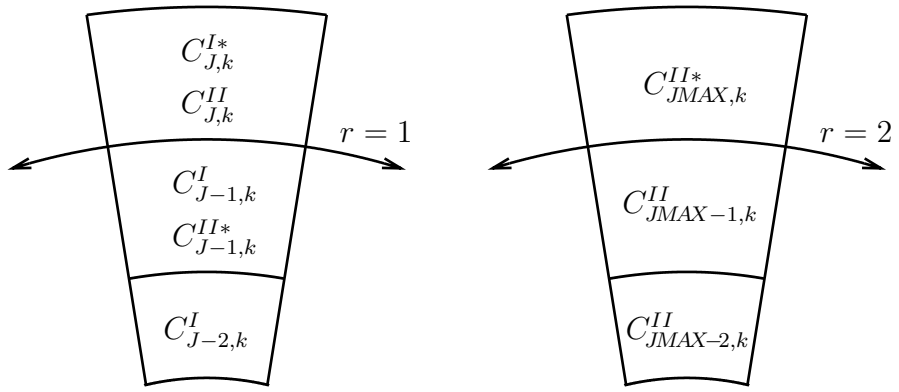

(a) boundary between the drop and magma

(b) external boundary

Figure 3.2: Imaginary concentrations (denoted by an asterisk) in the 2D spherical grid. Vertical arrow designates interface.

3.3.1 Discretization at the metal-silicate interface

At the interface between the drop and the silicates we impose the partition coefficient (2.10) and continuity of the radial flux (2.11). Using discretization (3.10) and (3.11) we evaluate the concentration in the imaginary cells as follows

$$C^{\mathrm{I}*}_{J,k} = \frac{2K}{1+K\mathcal{R}_{\mathrm{D}}} C^{\mathrm{II}}_{J,k} - \frac{1-K\mathcal{R}_{\mathrm{D}}}{1+K\mathcal{R}_{\mathrm{D}}} C^{\mathrm{I}}_{J-1,k}\,, \tag{3.23}$$

$$C^{\mathrm{II}*}_{J-1,k} = \frac{1-K\mathcal{R}_{\mathrm{D}}}{1+K\mathcal{R}_{\mathrm{D}}} C^{\mathrm{II}}_{J,k} + \frac{2\mathcal{R}_{\mathrm{D}}}{1+K\mathcal{R}_{\mathrm{D}}} C^{\mathrm{I}}_{J-1,k}\,. \tag{3.24}$$

3.3.2 Discretization at the external boundary

At the front of the drop, for $\theta \in (0, \frac{\pi}{2})$, we impose constant concentration (2.12) that results in

$$C^{\mathrm{II}*}_{JMAX,k} = 2C_{\mathrm{ext}} - C^{\mathrm{II}}_{JMAX-1,k}\,, \tag{3.25}$$

for the concentration in the imaginary cell.

For $\theta \in (\frac{\pi}{2}, \pi)$ condition (2.14) and discretization (3.11) involves six discrete cells $C^{\mathrm{II}}_{JMAX-1,k}$, $C^{\mathrm{II}}_{JMAX-1,k\pm1}$, $C^{\mathrm{II}*}_{JMAX,k}$ and $C^{\mathrm{II}*}_{JMAX,k\pm1}$. However, concentration $C^{\mathrm{II}*}_{JMAX,k+1}$ and $C^{\mathrm{II}}_{JMAX-1,k+1}$ are not known at the time of computing $C^{\mathrm{II}}_{JMAX-1,k}$. It is thus necessary to introduce one-side discretization for a gradient of an angular part

$$(\partial_\theta C)^{\mathrm{ext}} = \frac{1}{2d\theta}(3C^{\mathrm{ext}}_{j,k} - 4C^{\mathrm{ext}}_{j,k-1} + C^{\mathrm{ext}}_{j,k-2})\,, \tag{3.26}$$

with the second order accuracy. Index $(.)^{\mathrm{ext}}$ denotes that concentration is expressed on the external boundary. Assuming further discretization (3.10) we get for the imaginary cell

$$\begin{aligned} C^{\mathrm{II}*}_{JMAX,k} &= \frac{1-\frac{3\Delta r}{2v_r}\alpha}{1+\frac{3\Delta r}{2v_r}\alpha}\, C^{\mathrm{II}}_{JMAX-1,k} \\ &+ \frac{2\alpha}{\frac{v_r}{\Delta r}+\frac{3}{2}\alpha}\left(C^{\mathrm{II}}_{JMAX,k-1} + C^{\mathrm{II}}_{JMAX-1,k-1}\right) \\ &- \frac{\frac{1}{2}\alpha}{\frac{v_r}{\Delta r}+\frac{3}{2}\alpha}\left(C^{\mathrm{II}}_{JMAX,k-2} + C^{\mathrm{II}}_{JMAX-1,k-2}\right)\,, \end{aligned} \tag{3.27}$$

where $\alpha = \frac{v_\theta}{2\Delta\theta r_J}$.

Radial and angular part are thus no more independent through Eq. (3.27).

3.4 Resolution

Number of grid cells in the radial direction is picked so that there are at least three cells in the diffusion boundary layer, i.e., $JMAX = 6/\delta$. Further, number of tangential grid cells is identical to number of radial grid cells, i.e., $JMAX = KMAX$.

In order to estimate the time step Δt we consider the Courant-Fridrichs-Lewy condition. Since we use an implicit scheme in time domain we use the large time step when the Courant number is greater than one, i.e, $\frac{\Delta t|v|}{\Delta r} + \frac{\Delta t|v|}{r\Delta\theta} + \frac{\Delta t\mathcal{D}}{\Delta r^2} + \frac{\Delta t\mathcal{D}}{r\Delta r\Delta\theta} > 1$.

Despite the small values of the diffusion coefficients, the diffusion times are generally faster than the advection times.

3.5 Benchmarking

Numerical resolution consists of solving two diffusive-advective equations coupled by boundary conditions at the interface. There are two used schemes, namely the

central difference scheme and the central scheme, respectively, solving the diffusive and the advective part of the equations. Below, we present tests of each of them in the numerical code.

3.5.1 Benchmark of the diffusion scheme

In order to test the spatial central difference scheme we arrange an experiment of non-moving drop in a non-moving liquid ($v^{\mathrm{I}} = v^{\mathrm{II}} = 0$). We compute a steady state solution of diffusion equation with a unitary volume concentration sources, unitary diffusion coefficients and unitary partition coefficient K,

$$\frac{\partial C}{\partial t} = \nabla^2 C + 1\,. \tag{3.28}$$

Boundary condition is zero external concentration for $\theta \in (0, \pi)$. Figure 3.3 shows the analytical solution and the steady state limit of the numerical solution. Analytical solution C_{A} is given by $C_{\mathrm{A}} = \frac{1}{6}(1 - r^2)$.

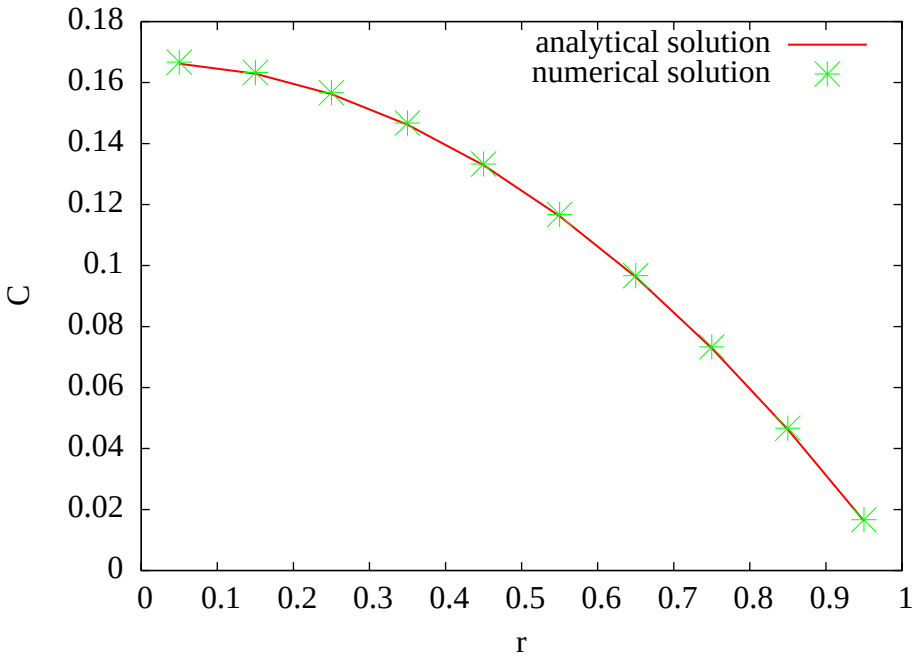

Figure 3.3: Comparison of numerical and analytical steady state solution of diffusion equation with concentration sources. The experiment was carried out with a mesh of 80×80 cells.

Discretization of all equations were done so as to attain second order spatial accuracy. Numerical solution C_{N} is thus characterized by algebraic convergence

$$||C_{\mathrm{N}} - C_{\mathrm{A}}||_{\mathcal{L}_2} \leq \Delta r^2\,. \tag{3.29}$$

In order to test Eq. (3.29) we set up experiment as described above and change a resolution of the grid Δr and $\Delta\theta$. Number of radial and tangential grid cells are identical for all experiments. Figure 3.4 shows the root mean square (rms) error as a function of the grid element Δr with the least squares fit $0.05(\Delta r)^{2.00}$. Acquired dependence complies thus with Eq. (3.29).

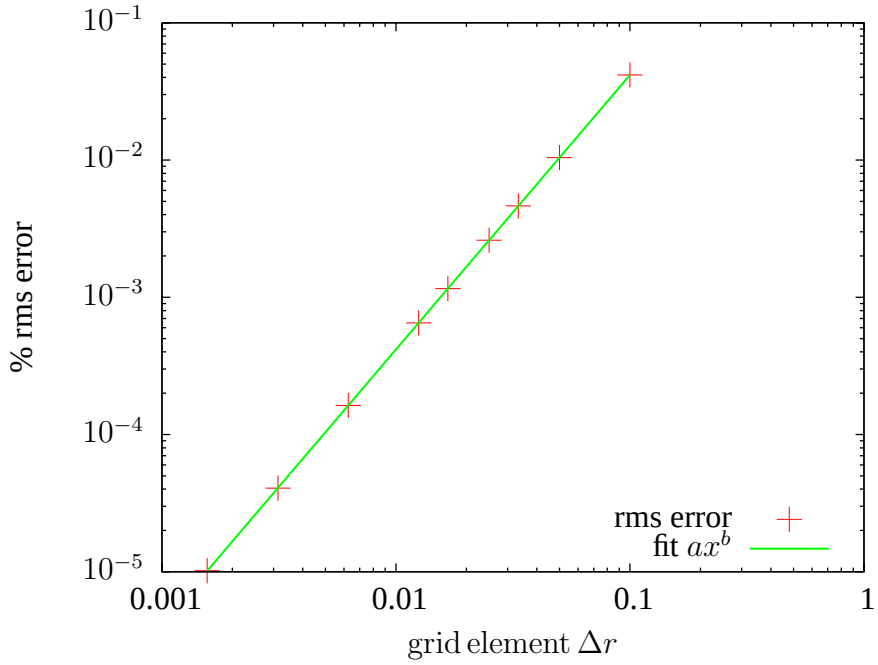

Figure 3.4: Log-log graph of a spatial convergence for a steady state solution of diffusion equation with concentration sources. Root mean square (rms) error is displayed as a function of a grid step Δr. Fitted parameters are $a = 0.05$, $b = 2.00$.

3.5.2 Benchmark of the advection scheme

The advection scheme was tested by calculating advection without concentration sources in the velocity field given by Eqs. (2.52) and (2.53). The initial concentration is 0.2 except circular region of radius 0.2 where concentration is 1. This initial concentration is advected by roughly $\pi/2$, then the velocity field is inversed to shift the concentration anomaly to the initial condition. The final concentration should be therefore identical to the initial state.

Figure 3.5 shows the results. As discussed in the previous section, an implicit scheme is used in time domain that allows to use Courant number greater that 1. Therefore the advection tests are performed for Courant number 1 and 10. The final and initial states are in a good agreement. The root mean square (rms) error for Courant number 1 is 0.01% ; the rms error for Courant number 10 is 0.1%. No nu-

merical diffusion appeared. However, numerical oscillations were presented within experiments.

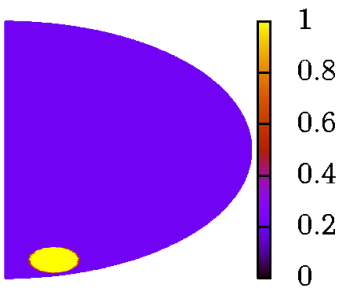

(a) initial concentration

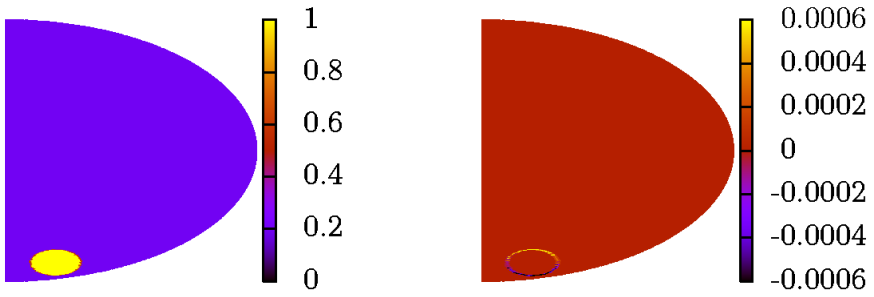

(b) final state (left fig.) and difference (final-initial) (right fig.) for Courant number = 1 ; rms error=0.01%

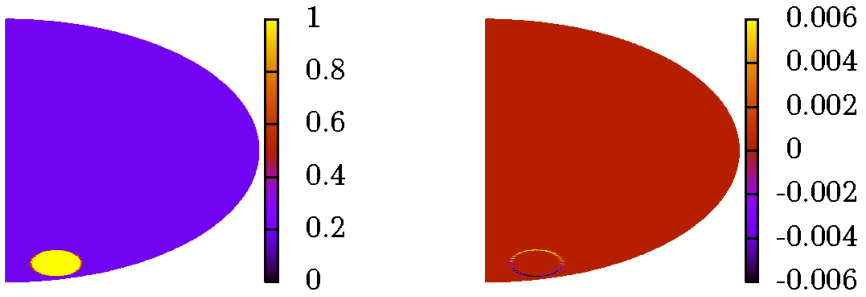

(c) final state (left fig.) and difference (final-initial) (right fig.) for Courant number = 10 ; rms error=0.1%

Figure 3.5: Test of the advection scheme. (a) Initial concentration. (b) and (c) Concentration after the anomaly was advected about $\pi/2$ and shifted back to the initial position (left column) for two different Courant numbers. Right column shows the difference of final and initial concentration distribution. Calculations were done on a grid of 400×400 cells.

Chapter 4

Results

In this chapter we present the results of our numerical simulations. We perform the calculations for the constant partition coefficient with the Peclet numbers up to 10^5. We compute the characteristic times of equilibration for different parameter sets in order to determine the time scaling laws and estimate the significance of the viscosity ratio.

4.1 Numerical experiments

We study the equilibration times of the heterogeneous system described in Chapter 2. In order to compute the evolution of metal-silicate equilibration we use the code established in Chapter 3.

We characterize the concentration within the drop by its mean value $\langle C \rangle = \frac{1}{V} \int_V C \, \mathrm{d}V$, where V is the volume of the drop. Analytical analysis in Section 2.6 suggests that the evolution of concentration follows exponential law

$$\langle C \rangle \sim \exp\left(-\frac{t}{\tau}\right) , \tag{4.1}$$

where τ is the characteristic time. It is thus τ that controls how long does it take to change the system from a non-equilibrium condition to equilibrium condition.

We initiate the experiment from non-equilibrium, imposing concentration 1 within the drop and 0 outside, respectively. Figure 4.1 shows several snapshots from the time evolution of concentration for one particular setup. Note the depletion of concentration in the blob and its advection through the upper boundary out of the computational domain.

Acquired time evolution is then fitted by exponential curve using two free parameters, the pre-exponential factor and the characteristic time. The least squares fit is computed using the `Gnuplot` program. The relative standard deviations (RSD) don't exceed 0.32% for the fitted parameters within all experiments. Exponential regression thus corresponds very well with the character of time evolution of concentration.

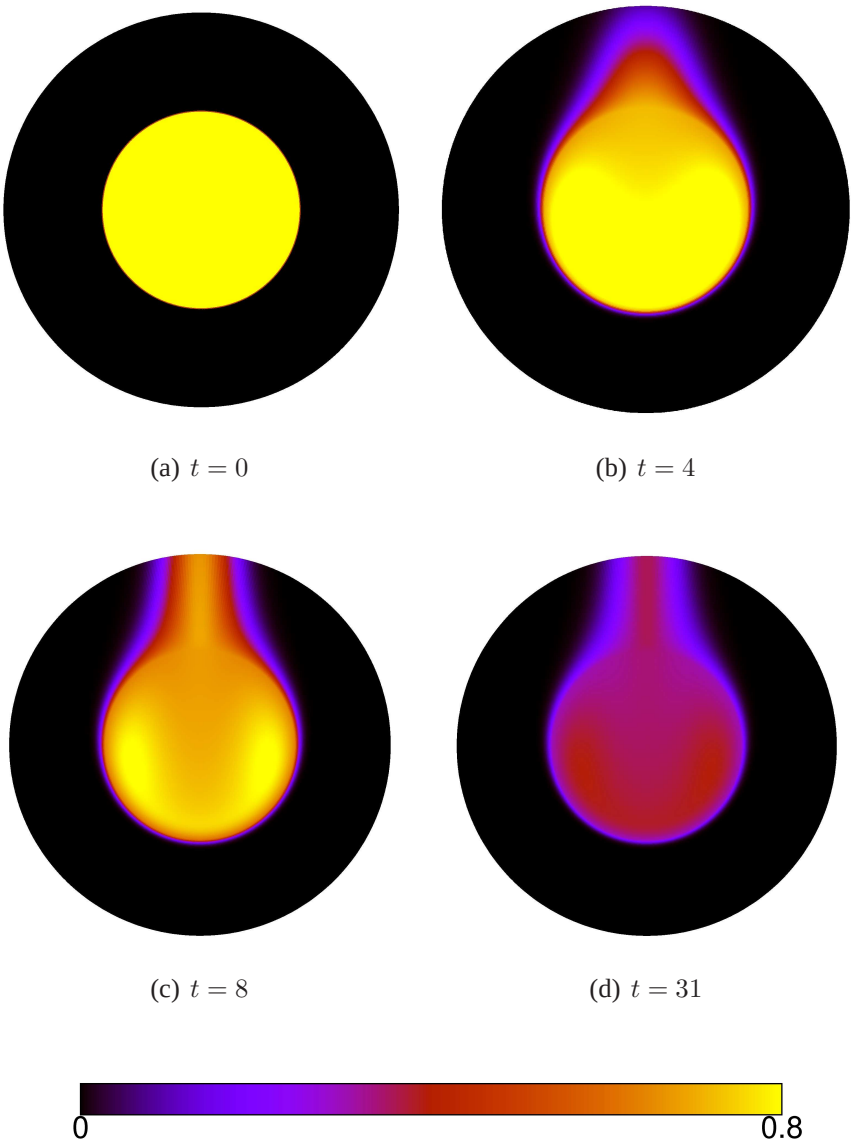

(a) $t = 0$ (b) $t = 4$

(c) $t = 8$ (d) $t = 31$

Figure 4.1: Snapshots of evolution of concentration for one particular run with following parameters: $\mathrm{Pe} = 1.3{\cdot}10^3$, $\mathcal{R}_\mu = 10^{-2}$, $\mathcal{R}_\mathrm{D} = 10$, and $K = 1$. Initial concentration is 1 within the drop and 0 outside. Characteristic time is $\tau = 31$. Computed on a grid with 200×200 cells with the Courant number 100.

Once we have τ for several experiments we study its dependence on the Peclet number in order to develop a predictive tool that could be used for the Earth's conditions.

We have three dimensionless parameters that fully describe the system as indicated in Section 2.5. In order to establish the effect of viscosity we set up a range of experiments with the same diffusion ratio $\mathcal{R}_\mathrm{D}$, and vary the Peclet number Pe and the ratio

of viscosities $\mathcal{R}_\mu$.

Parameters of the system are listed in Table 4.1. All runs were computed for the stable size of the drop given by Eq. (2.86). We consider that diffusion is thousand times faster in metal than in silicates, diffusion ratio is thus $\mathcal{R}_\mathrm{D} = 10^3$. Further, we impose the unit partition coefficient $K = 1$.

quantity	**value**
density of iron ρ^I	$7800\,\mathrm{kg\,m^{-3}}$
density of silicates ρ^II	$3750\,\mathrm{kg\,m^{-3}}$
gravity g	$10\,\mathrm{m\,s^{-2}}$
surface tension of iron γ	$1\,\mathrm{N\,m^{-1}}$

Table 4.1: Parameters of the system.

Figure 4.2 shows the dimensionless characteristic time as a function of the Peclet number for six different viscosity ratios varying from $\mathcal{R}_\mu = 10^{-3}$ to $\mathcal{R}_\mu = 10^3$. The final dependence is fitted by $\tau = \alpha(\mathrm{Pe})^\beta$ using two free parameters α and β. Table 4.2 summarises the results of fitted parameters. The results of pre-factor α_A of an analytical model established in section 2.6, see Eq. (2.80), is listed in the same table as well.

For the viscosity ratio less then $\mathcal{R}_\mu = 10^{-1}$ the characteristic time is proportional to $\sim (\mathrm{Pe})^{1/2}$ that is in a good agreement with the analytical model. The power of the Peclet number rises with the rising viscosity ratio up to $\beta = 0.65$ for $\mathcal{R}_\mu = 10^3$. Considering the ratio of velocities within the drop and outside, cf. Figure 2.5, the mixing within the drop is more efficient for the low viscosity ratio that speeds up importantly the equilibration rate.

Figure 4.3 shows the characteristic time as a function of viscosity ratio for the Peclet number $\mathrm{Pe} = 10^4$. For low viscosity ratios the characteristic time remains the same. For high viscosity ratios the significant increase of τ is clearly visible reflecting the inefficient stirring within the blob as noted above.

4.2 Liquid vs. rigid blob

The results of the previous section suggest to compare the characteristic times of liquid and rigid blob. We thus arrange an experiment of rigid drop falling in a silicate magma. The velocity field outside the drop is given by Eqs. (2.56) and (2.57), the Stokes terminal velocity is given by Eq. (2.55).

Initial conditions are the unitary concentration within the drop and zero concentration outside. Ratio of diffusion coefficients is kept constant within all experiments, $\mathcal{R}_\mathrm{D} = 10^3$. Partition coefficient one is imposed.

Figure 4.4 shows the characteristic times as a function of the Peclet number in comparison with the results of falling liquid drop for two different viscosity ratios. Final fitted parameters for liquid and rigid drop are listed in Table 4.3.

$\mathcal{R}_\mu$	α	β	α_{A}
10^{-3}	0.72	0.50	0.72
10^{-2}	0.72	0.50	0.73
10^{-1}	0.75	0.50	0.76
10^{1}	1.10	0.56	2.40
10^{2}	0.68	0.64	7.27
10^{3}	0.62	0.65	22.89

Table 4.2: Fitted parameters α and β of the equation for the characteristic time $\tau = \alpha(\mathrm{Pe})^{\beta}$ for different viscosity ratios $\mathcal{R}_\mu$. Diffusion ratio is kept constant within all experiments ; $\mathcal{R}_{\mathrm{D}} = 1000$. Partition coefficient one is imposed. The pre-factor of analytical model α_{A} is listed in the fourth column.

The character of equilibration of the liquid sphere tends to the equilibration character of the solid drop with increasing viscosity ratio as is already suggested by Figures 2.3 and 2.5 since the stirring within the blob becomes ineffective for high viscosity ratio.

The characteristic time of the rigid blob depends on the Peclet number with the power of 2/3 that is in a good agreement with the analytical model proposed in Chapter 2. Comparing the pre-factors of the scaling power law we get 0.52 for the analytical model and 0.60 for the numerical model.

$\mathcal{R}_\mu$	α	β	
10^{-2}	0.72	0.50	liquid
10^{2}	0.68	0.64	liquid
	0.60	0.66	rigid

Table 4.3: Fitted parameters α and β of the equation for the characteristic time $\tau = \alpha(\mathrm{Pe})^{\beta}$ for liquid and rigid drop. Diffusion ratio is kept constant ; $\mathcal{R}_{\mathrm{D}} = 1000$. Partition coefficient one is imposed.

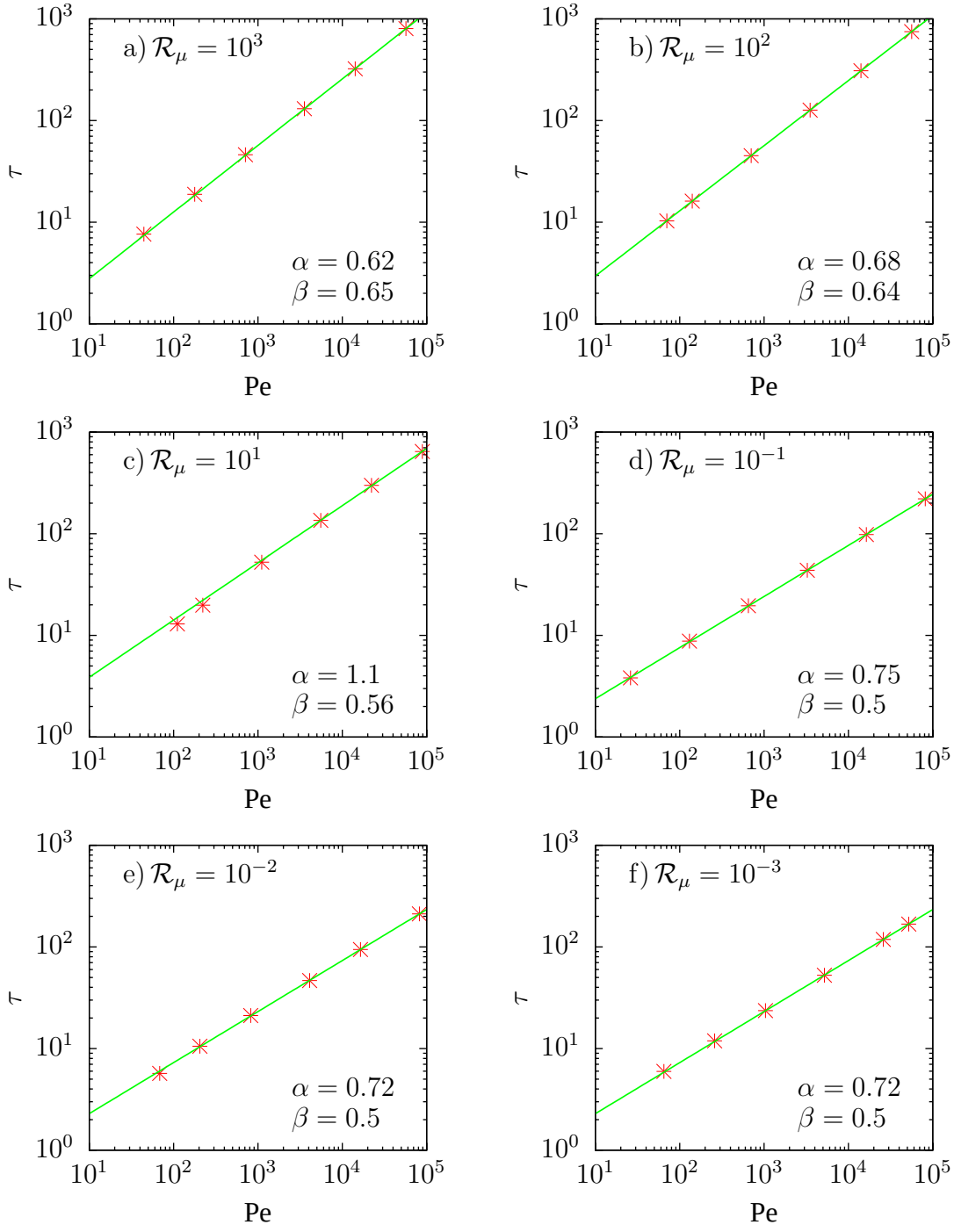

Figure 4.2: Non-dimensional characteristic time τ as a function of the Peclet number Pe for different viscosity ratios. Ratio of diffusion coefficients is kept constant for all experiments (a)-(f) ; $\mathcal{R}_\mathrm{D} = 10^3$. Solid lines represent fits of function $\tau = \alpha\,(\mathrm{Pe})^\beta$. Parameters of the fits are displayed in the right bottom corner of each figure.

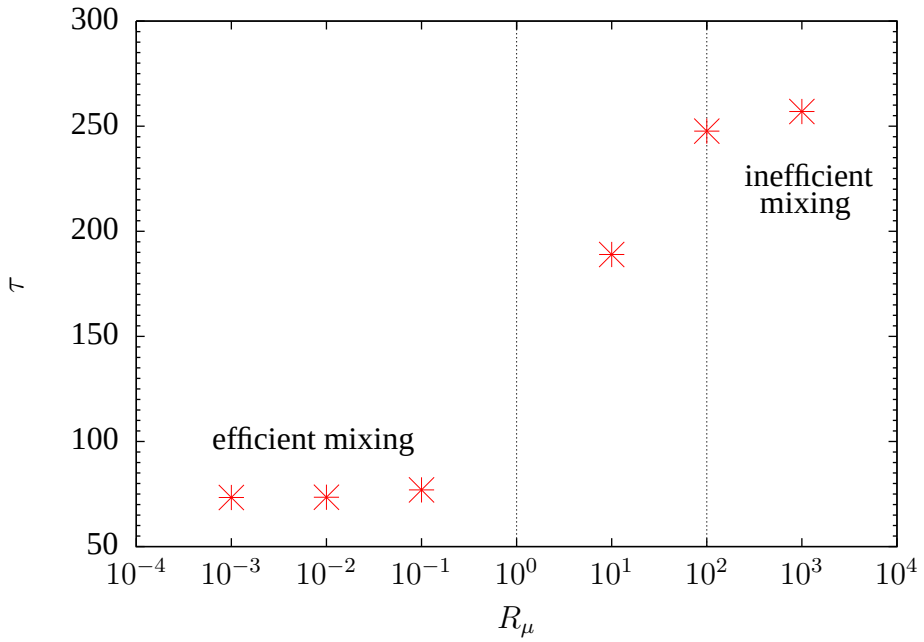

Figure 4.3: Characteristic time τ as a function of viscosity ratio $\mathcal{R}_\mu$ for $\mathrm{Pe} = 10^4$ and $K = 1$. Dashed vertical lines depict areas with different efficiency of stirring within the blob.

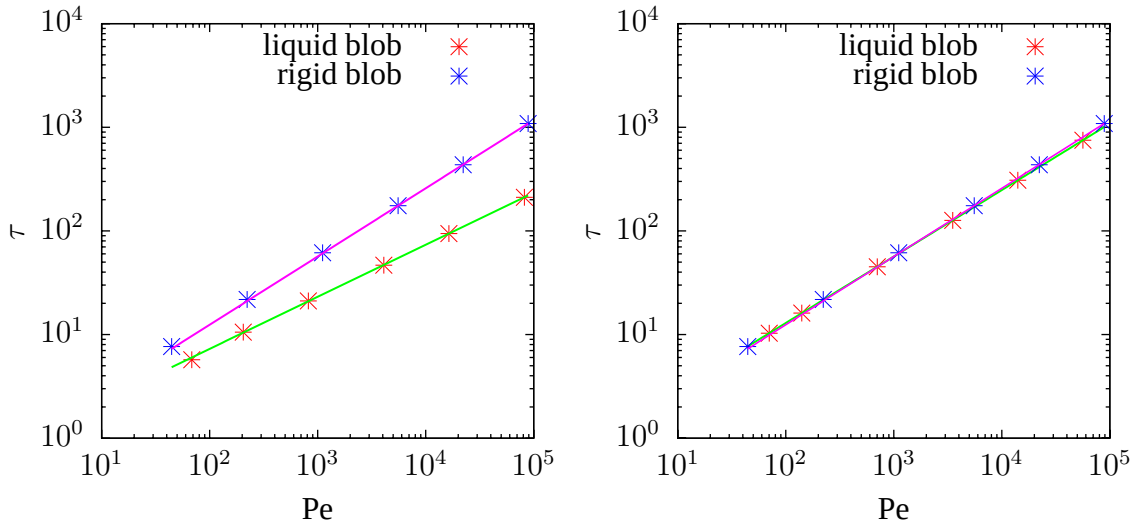

(a) viscosity ratio $\mathcal{R}_\mu = 10^{-2}$ **(b)** viscosity ratio $\mathcal{R}_\mu = 10^{2}$

Figure 4.4: Non-dimensional characteristic time τ as a function of the Peclet number Pe for liquid and rigid drop. Comparison for two different viscosity ratios $\mathcal{R}_\mu$ is displayed. Ratio of diffusion coefficients and the partition coefficient are kept constant ; $\mathcal{R}_\mathrm{D} = 10^3$ and $K = 1$. Solid lines represent fits of function $\tau = \alpha\,(\mathrm{Pe})^\beta$.

Chapter 5

Discussion

In the previous chapters we developed an analytical model and a numerical model for time evolution of equilibration between an iron drop and surrounding silicates. Numerical simulations, performed for the Peclet numbers up to 10^5, match the theoretically predicted characteristic times. We thus validate our analytical model and can use the proposed scaling laws for high Peclet numbers corresponding to the Earth's conditions.

The model is more accurate for the high diffusion ratios since we match the concentration at the surface of the drop with the average concentration within the blob, see Eq. (2.77), that is plausible for high metal diffusion or efficient inner circulation.

The numerical model allowed us to determine two different equilibration regimes. For low viscosity ratios the stirring within the blob efficiently accelerates the equilibration and the blob follows the dimensionless scaling law $\tau = \alpha_1(\mathrm{Pe})^{1/2}$. For high viscosity ratios mixing within the blob becomes less efficient and the equilibration rate approaches the equilibration rate of the rigid drop and allows for the $\tau = \alpha_2(\mathrm{Pe})^{2/3}$ scaling law. The transition between the different regimes occurs in a window when $\mathcal{R}_\mu \in (10^0, 10^2)$.

Considering the normalization of time by the advective factor R/U we can formulate the scaling laws with physical dimensions whereby we predict the dimensional τ for the primitive Earth as functions of magma ocean parameters and the droplet parameters. The results are displayed in Figure 5.1 where we used $\alpha_1 = 0.72$ and $\alpha_2 = 0.6$. Results won't change much with other pre-factors α_1 or α_2. What is important is the power of the Peclet number. We allow for iron viscosity $\mu^{\mathrm{I}} = 1\,\mathrm{Pa\,s}$ that corresponds to high pressure conditions.

Allowing for the silicate viscosity $10^2\,\mathrm{Pa\,s}$ that corresponds to high pressure conditions [13] the stable size of the drop is $7\,\mathrm{cm}$ with the terminal velocity $0.2\,\mathrm{m\,s^{-1}}$. Characteristic time of equilibration is then $1.3 \cdot 10^4\,\mathrm{s}$ and the equilibration distance that the drop reaches within the τ is $3\,\mathrm{km}$ when we allowed for the silicate diffusion coefficient $D^{\mathrm{II}} = 10^{-12}\mathrm{m^2\,s^{-1}}$.

For the silicate viscosity $10^{-2}\,\mathrm{Pa\,s}$ that corresponds to high temperature conditions [13] the drop radius is $0.1\,\mathrm{cm}$ and it falls with velocity $1\,\mathrm{m\,s^{-1}}$. The characteristic time of equilibration is $8 \cdot 10^2\,\mathrm{s}$ and the equilibration distance is $1\,\mathrm{km}$ when we allowed for the same silicate diffusion coefficient as before.

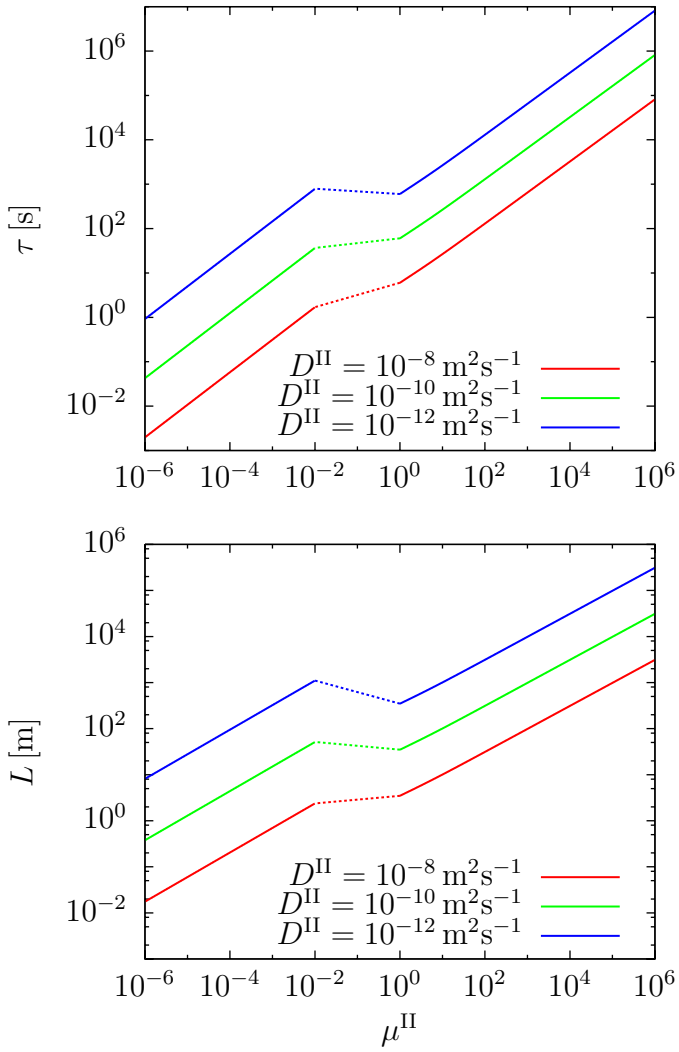

Figure 5.1: Dimensional characteristic time (upper figure) and corresponding equilibration distance (bottom figure) as functions of the silicate viscosity for three different diffusion coefficients. Iron viscosity is $\mu^{\mathrm{I}} = 1\,\mathrm{Pa\,s}$, partition coefficient is $K = 1$. The solid lines indicate two regimes. In the first regime, for silicate viscosities larger than the iron viscosity, the stirring within the drop is efficient. In the second regime, for silicate viscosities less than one percent of the iron viscosity, mixing within the blob is inefficient. The transition in between is indicated by the dashed lines.

In these two cases the equilibrium of the drop sinking in the magma ocean with depth about $700\,\mathrm{km}$ was attained. However, the characteristic times can be significantly enhanced by several orders by the different partitioning. E.g. partition coefficient $K = 500$ will $500\times$ lengthen the characteristic times, see Eqs. (2.80) and (2.83). Then, only for low silicate viscosity the metal-silicate equilibrium was reached.

Our numerical model is based on several simplifying assumptions. We assume that the infinite space of the magma ocean can be replaced by a sphere with radius $2R$. For the runs with the lowest Peclet numbers, i.e., the highest diffusion rates, the thickness of the boundary layer is five times smaller than the radius of the drop. The boundary layer is thus sufficiently thin to consider that our approximation is accurate.

Next, we assume that magma ocean is in a regime of laminar convection. The metal segregates thus with the R-H terminal velocity given by Eq. (2.54). However, the magma ocean could be in a regime of vigorous convection and the drag force should be thus considered when estimating the terminal velocity since the flow around the droplet is likely turbulent. The terminal velocities are then about $\sim 10\times$ smaller [2]. Moreover, because of high convection velocities ($\sim 10\,\mathrm{m\,s^{-1}}$), iron droplets may remain entrained for a significant time in the magma ocean instead of falling straightforward to the bottom [21].

We also suppose that the drop doesn't deform and keeps its shape. In fact, "lentil" like flattering likely occurs but it would be a different task to investigate. Finally, we didn't consider the Rayleigh-Taylor instability caused by the inertia when estimating the stable size of the drop.

Considering the numerical side of the task, the problem is intensive in number of iterations needed to achieve the equilibrium. The choice of numerical scheme then becomes crucial. The implicit method in time domain enables us to use large Courant number and substantially shorten computation times.

Chapter 6

Conclusions

In this thesis we developed a model for the chemical equilibration of small metal droplets with surrounding silicates that likely occurred in the primitive Earth within the core formation event.

In order to study the chemical evolution of metal droplets dispersed in the magma ocean we proposed an analytical and numerical models that consider the simple blob sinking with a constant terminal velocity in the host liquid.

The stable size of the drop is given by the critical Weber number that reflects the density ratio of the two liquids. The size of the drop varies from micrometers for low silicate viscosity to meters for high silicate viscosity. The smallest droplets sink with the highest terminal velocity reaching up to tens of meters per second.

We studied the characteristic times of chemical equilibration. The rate of equilibration is given by the size of the drop and efficiency of mixing within the drop. There are two regimes of equilibration: for low silicate viscosity (compared to the iron viscosity), the droplet is small and though it falls with high terminal velocity, the stirring within the blob is inefficient and the equilibration rate is controlled either by the diffusion in silicates or by the diffusion in metal. For high silicate viscosity (compared to the iron viscosity), large, slow settling droplets are established with efficient inner circulation. The concentration is then rapidly homogenized and the equilibration rate is thus controlled by the diffusion of silicates. The numerical code enabled us to determine the transition between the two regimes which occurs in a narrow window for silicate viscosity less than the iron viscosity and higher than the one percent of the iron viscosity.

We proposed scaling laws for the characteristic time of equilibration. The scaling is based on the boundary layer analysis and confirmed by the full numerical solution of the advective–diffusive equations for the Peclet numbers up to 10^5. Hence, we can predict the characteristic times of the equilibration of small droplets in the magma ocean as functions of the magma ocean and droplet parameters.

The higher the silicate viscosity the larger the characteristic time. The equilibration times are short that supports the idea that the drops fully equilibrated while sinking. That is in agreement with [20].

Continuing in work will consist of running experiments with depth-dependent partition coefficient. In the reference system of the droplet, this case corresponds to time-dependency of the partition coefficient. It will be also useful to incorporate the drag coefficient into the equation of motion and include thus the influence of the drag force.

Appendix A

Differential operators in axi-symmetric spherical coordinates

For convenience of the reader we bring the list of the differential operators in axi-symmetric spherical coordinates that were used within the presented text. The complex overview can be found e.g. in [14].

Gradient of scalar

$$\nabla f(r,\theta) = \left(\frac{\partial f}{\partial r}, \frac{1}{r}\frac{\partial f}{\partial \theta}\right) \tag{A.1}$$

Divergence of vector

$$\nabla \cdot \boldsymbol{F}(r,\theta) = \frac{1}{r^2}\frac{\partial (r^2 F_r)}{\partial r} + \frac{1}{r\sin\theta}\frac{\partial (F_\theta \sin\theta)}{\partial \theta} \tag{A.2}$$

Laplace of scalar

$$\nabla^2 f = \frac{1}{r^2}\frac{\partial}{\partial r}\left(r^2 \frac{\partial f}{\partial r}\right) + \frac{1}{r^2\sin\theta}\frac{\partial}{\partial \theta}\left(\sin\theta \frac{\partial f}{\partial \theta}\right) \tag{A.3}$$

Laplace of vector

$$\left(\nabla^2 \boldsymbol{F}\right)_r = \nabla^2 F_r - \frac{2}{r^2}F_r - \frac{2}{r^2\sin\theta}\frac{\partial}{\partial\theta}\left(F_\theta \sin\theta\right) \tag{A.4}$$

$$\left(\nabla^2 \boldsymbol{F}\right)_\theta = \nabla^2 F_\theta - \frac{1}{r^2\sin^2\theta}F_\theta + \frac{2}{r^2}\frac{\partial F_r}{\partial\theta} \tag{A.5}$$

Curl operator

$$\left(\nabla \times \boldsymbol{F}\right)_r = \frac{1}{r\sin\theta}\frac{\partial}{\partial\theta}(F_\phi \sin\theta) \tag{A.6}$$

$$\left(\nabla \times \boldsymbol{F}\right)_\theta = -\frac{1}{r}\frac{\partial}{\partial r}\left(rF_\phi\right) \tag{A.7}$$

$$\left(\nabla \times \boldsymbol{F}\right)_\phi = \frac{1}{r}\left(\frac{\partial}{\partial r}(rF_\theta) - \frac{\partial F_r}{\partial\theta}\right) \tag{A.8}$$

Bibliography

[1] G. K. Batchelor. *An Introduction to Fluid Dynamics*. Cambridge, UK: Cambridge University Press, February 2000.

[2] P. P. Brown and D. Lawler. Sphere Drag and Settling Velocity Revisited. *Journal of Environmental Engineering*, 129:222–231, March 2003.

[3] N. L. Chabot, D. S. Draper, and C. B. Agee. Conditions of core formation in the earth: Constraints from Nickel and Cobalt partitioning. *Geochim. Cosmochim. Acta*, 69:2141–2151, April 2005.

[4] A. Corgne, S. Keshav, B. J. Wood, W. F. McDonough, and Y. Fei. Metal silicate partitioning and constraints on core composition and oxygen fugacity during Earth accretion. *Geochim. Cosmochim. Acta*, 72:574–589, January 2008.

[5] J. Crank and P. Nicolson. A practical method for numerical evaluation of solutions of partial differential equations of the heat–conduction type. *Proceedings of the Cambridge Philosophical Society*, 43:50–67, 1947.

[6] D. P. Dobson, J. P. Brodholt, L. Vočadlo, and W. A. Crichton. Experimental verification of the Stokes-Einstein relation in liquid Fe-FeS at 5 GPa. *Molecular Physics*, 99:773–777(5), May 2001.

[7] J. Douglas. On the numerical integration of $\frac{\partial^2 u}{\partial x^2} + \frac{\partial^2 u}{\partial y^2} = \frac{\partial u}{\partial t}$ by implicit methods. *Journal of the society for industrial and applied mathematics*, 3:42–65, 1955.

[8] R. D. Duan, S. Koshizuka, and Y. Oka. Numerical and theoretical investigation of effect of density ratio on the critical weber number of droplet breakup. *Journal of nuclear science and technology*, 40:501–508, July 2003.

[9] O. Grasset and F. Albarede. Hybridization of mingling magmas with different densities. *Earth and Planetary Science Letters*, 121:327–332, February 1994.

[10] A. N. Halliday. *The Origin and Earliest History of the Earth*, volume 1, pages 509–557. Treatise on Geochemistry: Meteorites, Comets and Planets, edited by A. M. Davis, H. D. Holland and K. K. Turekian. Elsevier Ltd., December 2005.

[11] Veniamin G. Levich. *Physicochemical Hydrodynamics*. Prentice–Hall, Englewood Cliffs, N.J., 1964.

[12] J. Li and C. B. Agee. The effect of pressure, temperature, oxygen fugacity and composition on partitioning of nickel and cobalt between liquid Fe-Ni-S alloy and liquid silicate: implications for the earth's core formation. *Geochim. Cosmochim. Acta*, 65:1821–1832, June 2001.

[13] C. Liebske, B. Schmickler, H. Terasaki, B. T. Poe, A. Suzuki, K.-I. Funakoshi, R. Ando, and D. C. Rubie. Viscosity of peridotite liquid up to 13 GPa: Implications for magma ocean viscosities. *Earth and Planetary Science Letters*, 240:589–604, December 2005.

[14] Z. Martinec. *Continuum mechanics (Lecture notes)*. `http://geo.mff.cuni.cz/vyuka.htm`, May 2003.

[15] K. Nomura, S. Koshizuka, Y. Oka, and H. Obata. Numerical analysis of droplet breakup behaviour using particle method. *Journal of nuclear science and technology*, 38:1057–1064, December 2001.

[16] D.W. Peaceman and H.H. Rachford. The numerical solution of parabolic and elliptic differential equations. *Journal of the Society for industrial and Applied Mathematics*, 3:28–41, 1955.

[17] W. H. Press, S. A. Teukolsky, W. T. Vetterling, and B. P. Flannery. *Numerical recipes in FORTRAN. The art of scientific computing*. Cambridge: University Press, 2nd ed., 1992.

[18] K. Righter and M. J. Drake. Metal-silicate equilibrium in a homogeneously accreting earth: new results for Re. *Earth and Planetary Science Letters*, 146:541–553, February 1997.

[19] K. Righter and M. J. Drake. Effect of water on metal-silicate partitioning of siderophile elements: a high pressure and temperature terrestrial magma ocean and core formation. *Earth and Planetary Science Letters*, 171:383–399, September 1999.

[20] D. C. Rubie, H. J. Melosh, J. E. Reid, C. Liebske, and K. Righter. Mechanisms of metal–silicate equilibration in the terrestrial magma ocean. *Earth and Planet. Sci. Lett.*, 205:239–255, January 2003.

[21] D. C. Rubie, F. Nimmo, and H. J. Melosh. *Formation of Earth's Core*, volume 9, pages 51–90. Treatise on Geophysics: Evolution of the Earth, edited by editor–in–chief G. Schubert and volume editor D. Stevenson. Elsevier Ltd., 2007.

[22] V. Solomatov. *Magma Oceans and Primordial Mantle Differentiation*, volume 9, pages 92–119. Treatise on Geophysics: Evolution of the Earth, edited by editor–in–chief G. Schubert and volume editor D. Stevenson. Elsevier Ltd., 2007.

[23] D. J. Stevenson. *Fluid Dynamics of a core formation*, pages 231–249. Origin of the Earth, edited by H. E. Newsom and J. H. Jones. New York: Oxford Univ. Press., p. 231–249, 1990.

[24] D. J. Stevenson. *Earth Formation and Evolution*, volume 9, pages 1–50. Treatise on Geophysics: Evolution of the Earth, edited by editor–in–chief G. Schubert and volume editor D. Stevenson. Elsevier Ltd., 2007.

[25] W. B. Tonks and H. J. Melosh. Core formation by giant impacts. *Icarus*, 100:326–346, December 1992.

[26] D. L. Turcotte and G. Schubert. *Geodynamics*. pp. 472. Cambridge, UK: Cambridge University Press, March 2002.

[27] Patankar Suhas V. *Numerical heat transfer and fluid flow*. Series in computational methods in mechanics and thermal sciences. Hemisphere Publishing Corporation, 1980.